

# Sedimentation of a dilute suspension of rigid spheres at intermediate Galileo numbers: the effect of clustering upon the particle motion

Markus Uhlmann\* and Todor Doychev†

Institute for Hydromechanics, Karlsruhe Institute of Technology  
76131 Karlsruhe, Germany

## Abstract

Direct numerical simulation of the gravity-induced settling of finite-size particles in triply-periodic domains has been performed under dilute conditions. For a single solid-to-fluid density ratio of 1.5 we have considered two values of the Galileo number corresponding to steady vertical motion ( $Ga = 121$ ) and to steady oblique motion ( $Ga = 178$ ) in the case of one isolated sphere. For the multi-particle system we observe strong particle clustering only in the latter case. The geometry and time scales related to clustering are determined from Voronoï tessellation and particle-conditioned averaging. As a consequence of clustering, the average particle settling velocity is increased by 12% as compared to the value of an isolated sphere; such a collective effect is not observed in the non-clustering case. By defining a local (instantaneous) fluid velocity average in the vicinity of the finite-size particles it is shown that the observed enhancement of the settling velocity is due to the fact that the downward fluid motion (with respect to the global average) which is induced in the cluster regions is preferentially sampled by the particles. It is further observed that the variance of the particle velocity is strongly enhanced in the clustering case. With the aid of a decomposition of the particle velocity it is shown that this increase is due to enhanced fluid velocity fluctuations (due to clustering) in the vicinity of the particles. Finally, we discuss a possible explanation for the observation of a critical Galileo number marking the onset of clustering under dilute conditions.

## 1 Introduction

The gravity-driven motion of heavy particles in a viscous fluid is a process which is relevant to many applications, such as precipitation in meteorology, waste water treatment, fluvial geomorphology and chemical engineering systems. In the general case the interaction between the fluid phase and the suspended inclusions is highly complex, involving a large range of spatial and temporal scales. Correspondingly, sedimenting suspensions exhibit a rich set of dynamical features which can significantly affect their global properties. Questions of practical interest with respect to such systems include the following: what is the average settling velocity of the particles? What are the particularities of their spatial distribution? What are the characteristics of the flow field induced by the particle motion?

Compared to the very idealized situation of a single fixed sphere in a uniform flow at low Reynolds number, the additional complexity when treating sedimenting suspensions stems from the combined effects of larger Reynolds numbers, particle mobility as well as from the multi-particle collective. The Reynolds number effect by itself has been extensively studied in the past (e.g. Johnson & Patel, 1999; Ghidersa & Dušek, 2000; Schouveiler & Provensal, 2002; Bouchet

---

\*markus.uhlmann@kit.edu

†todor.doychev@kit.edu

*et al.*, 2006). The picture that has emerged from these and other investigations of single fixed spheres in uniform, unbounded flow is as follows. With increasing Reynolds number the wake – which is axi-symmetric and steady at low Reynolds number – first undergoes a bifurcation which breaks the axi-symmetry while steadiness is maintained (above  $Re_{c1} \approx 210$ , where  $Re$  is based upon the magnitude of the unperturbed flow velocity  $u_\infty$ , the sphere diameter  $D$  and the kinematic fluid viscosity  $\nu$ ), leading to a wake structure in the shape of double-threaded vortices exhibiting a planar symmetry. Above a second critical value ( $Re_{c2} \approx 275$ ) the flow becomes unsteady and time-periodic, with vortex shedding taking place. Further increasing the Reynolds number leads to a loss of planar symmetry and of temporal periodicity (above  $Re_{c3} \approx 360$ ).

When allowing the sphere to move freely under the effect of gravity in an unbounded fluid initially at rest, new features emerge due to the additional degrees of freedom. In this case path instabilities arise in the coupled problem which is now described by two parameters, i.e. the solid to fluid density ratio  $\rho_p/\rho_f$  and the Galileo number  $Ga$  which is a measure for the ratio between gravitational and viscous forces acting on a submerged particle ( $Ga = u_g D/\nu$ , where  $u_g = (|\rho_p/\rho_f - 1| Dg)^{1/2}$  with  $g$  being the magnitude of the gravitational acceleration). In the two-parameter space a variety of particle path regimes are encountered, involving vertical, oblique, time-periodic oscillating, zig-zagging, helical and chaotic motion, as shown numerically (Jenny *et al.*, 2004) and experimentally (Veldhuis & Biesheuvel, 2007; Horowitz & Williamson, 2010). When focusing upon heavy particles (for which  $\rho_p/\rho_f > 1$ ) the bounds between the different regimes do not depend strongly upon the value of the density ratio. The sequence of regimes which is encountered as the Galileo number is increased from an initially small value (where steady motion along a vertical path is observed) leads to steady oblique motion, then to planar motion with periodic oscillations around an average oblique path, and finally to a breakdown of planar symmetry and time periodicity.

Much less is known about the behavior of multi-particle configurations. As a first step it is instructive to consider the case of several fixed spheres in certain spatial arrangements, thereby separating the pure collective effect from the pure effect of particle mobility. In this spirit, Tsuji *et al.* (1982) and Tsuji *et al.* (2003) have investigated a pair of spheres either aligned along the direction of the incoming flow or arranged transversally; Kim *et al.* (1993) and Schouveiler *et al.* (2004) have focused upon side-by-side configurations. In all these studies of fixed pairs of spheres the Reynolds number values were of the order of several hundred. It has been observed that the presence of a second sphere has a significant effect upon the wake structure and its stability properties, with correspondingly non-negligible influence on the drag and lift forces; this effect depends evidently upon the inter-particle distance and in a strong manner also upon the relative orientation of the particle pair.

The flow through random arrays of fixed spheres at Reynolds number values up to several hundreds has been investigated numerically by Hill *et al.* (2001), Beetstra *et al.* (2007) and Tennetti *et al.* (2011). The results of these studies have led to the establishment of different drag formulas given as a function of the solid volume fraction  $\Phi_s$  and of the Reynolds number. It should be noted that the range of solid volume fractions in the aforementioned studies was relatively large ( $\Phi_s \geq 0.1$ ). Contrarily, systematic direct numerical simulations or experiments considering the flow through randomly positioned (fixed) spheres at low solid volume fractions are not available to our knowledge. Riboux *et al.* (2013) have performed simulations of the flow through a random array of fixed spheres at low solid volume fractions (down to 0.006), however, deliberately under-resolving the flow in the vicinity of the spheres and explicitly imposing a time-dependency of the hydrodynamic particle force. They showed that their model nevertheless reproduces the large-scale features of the flow induced by laboratory bubble swarms relatively well. They were further able to separate the individual contributions to the amplitude of fluid velocity fluctuations stemming from the random wake positioning and from the temporal fluctuations of individual wakes.

Turning now to the case of gravity-induced sedimentation of many freely-mobile particles (i.e. where the effects of mobility and of the particle collective are present), a series of experiments have been carried out for solid volume fractions of  $\Phi_s \leq 0.0001$  and for Galileo numbers in the range of 40 to 340 by Parthasarathy & Faeth (1990*a,b*) and Mizukami *et al.* (1992). Under these very dilute conditions, reasonable predictions of the flow field induced by the particle ensemble

can be obtained when assuming a linear superposition of isolated particle wakes (with a suitable choice of the wake description).

To our knowledge [Kajishima & Takiguchi \(2002\)](#) were the first to perform direct numerical simulations of dilute sedimenting suspensions at particle Reynolds numbers of  $O(100)$  in periodic boxes. The numerical method was based upon fourth-order finite-differences on a non-conforming grid, representing the fluid-solid interface with the aid of a local marker function. For the sake of computational efficiency, however, the angular particle motion was initially not accounted for. They observed strong accumulation of particles (with a solid-to-fluid density ratio of 8.8) in columnar structures when the particle Reynolds number exceeded a value of 300. The appearance of clusters was shown to strongly enhance the average settling velocity of the particles. This result was explained by a wake attraction effect, where trailing particles experience lower drag, therefore accelerating and approaching the corresponding leading particles, resulting in locally enhanced concentrations of the solid phase. [Kajishima \(2004\)](#) later revisited the same configuration at a Reynolds number value of 300 (corresponding to  $Ga \approx 210$ ), now properly accounting for rotational particle motion. No clustering was observed for solid volume fraction values below 0.001. Furthermore, he found that the rotational motion of the particles plays a significant role in the regeneration cycle of particle clusters.

The problem of a large number of bubbles rising in an initially ambient fluid has received comparably more attention in the past. A few of the results from the literature on bubbles with relevance to solid particle sedimentation shall be mentioned in the following. Focusing on bubble Reynolds numbers of a few hundreds and volume fractions of the dispersed phase in the dilute regime, experiments have shown that the bubble wakes in a swarm are considerably attenuated as compared to isolated wakes, with an exponential decay of the velocity deficit reported by [Risso \*et al.\* \(2008\)](#). The energy spectrum of the bubble-induced liquid velocity fluctuations contains a significant range with a decay proportional to the inverse of the third power of the wavenumber ([Lance & Bataille, 1991](#); [Riboux \*et al.\*, 2010](#)). It was subsequently shown by [Risso \(2011\)](#) that such a spectral range may be explained by a superposition of localized random disturbances under certain conditions. Concerning the amplitude of the velocity fluctuations of the liquid carrier phase, it has been shown by [Risso & Ellingsen \(2002\)](#) and subsequent experiments ([Martinez-Mercado \*et al.\*, 2007](#); [Riboux \*et al.\*, 2010](#)) that it varies with a power of 0.4 of the disperse phase volume fraction.

This short summary shows that our understanding of dilute sedimenting suspensions at Reynolds numbers of the order of hundreds is still incomplete. Apart from the pioneering work of [Kajishima](#) and collaborators ([Kajishima & Takiguchi, 2002](#); [Kajishima, 2004](#)) the phenomenon of wake-induced clustering in this setting has received little attention. In particular, it is not known how particle clusters affect the scaling of the gravity-induced motion of both phases, i.e. the particle motion itself and the induced “pseudo-turbulence”. Furthermore, it is not clear whether (and to what extent) the larger set of results already obtained in the context of homogeneous bubbly flows apply to the case of heavy solid particles.

The objective of the present work is to provide a comprehensive description of the particle motion in dilute settling suspensions. The principal question which we attempt to solve is how the spatial distribution of the particulate phase affects its motion. We have simulated this configuration with full resolution of the fluid-solid interface by means of an immersed boundary method. Care has been taken to choose a small-scale resolution which is sufficient to resolve the details of the particle wakes at the respective Galileo number value. Large computational domain sizes were employed such as to allow for the characterization of large-scale features of the flow. In this study we focus upon a single value of the solid-to-fluid density ratio of 1.5 and upon a solid volume fraction of 0.005, while two values of the Galileo number are investigated, measuring 121 and 178. These two values correspond to the regimes where an isolated particle in an unbounded fluid exhibits a straight vertical path and to a steady oblique path, respectively. Here we find no significant particle clustering in the former case while massive clustering occurs in the latter one.

In the present paper the scope is limited to the analysis of the spatial distribution of the particles and of their motion. Detailed results relating to the flow field induced by the particle motion will be presented in a future publication.

The computational setup is described in the following section. The results of our simulations are then presented in § 3, where we first consider the temporal evolution of global quantities, before we turn to a Voronoi tessellation based analysis of the disperse phase distribution and finally to the particle motion. The paper closes with a summary and discussion in § 4.

## 2 Computational setup

### 2.1 Numerical method

The numerical method employed in the present simulations has been described in detail by Uhlmann (2005a). The incompressible Navier-Stokes equations are solved by a fractional step approach with an implicit treatment of the viscous terms (Crank-Nicolson) and a three-step Runge-Kutta scheme for the non-linear terms. The spatial discretization employs second-order central finite-differences on a staggered mesh which is uniform and isotropic. The no-slip condition at the surface of moving solid particles is imposed by means of a specifically designed immersed boundary technique (Uhlmann, 2005a). The motion of the particles is computed from the Newton equations for linear and angular motion of rigid bodies, driven by buoyancy, hydrodynamic force/torque and contact forces (in case of collisions). Since the suspension under consideration is dilute, collisions are treated by a simple repulsive force mechanism (Glowinski *et al.*, 1999) formulated such as to keep colliding particles from overlapping non-physically. In the multi-particle simulations presented herein it turns out that the average time interval between two collision events experienced by a particle measures 52 (39) times the gravitational time scale (in simulations M121 and M178, respectively, cf. table 1) showing that indeed collisions are relatively infrequent.

The computational code has been previously employed for the direct numerical simulation of various flow configurations (Uhlmann, 2008; Chan-Braun *et al.*, 2011; García-Villalba *et al.*, 2012; Kidanemariam *et al.*, 2013; Chan-Braun *et al.*, 2013).

### 2.2 Flow configuration and physical parameters

We consider the gravity-induced settling of multiple spherical particles with identical diameter in an otherwise ambient, incompressible, unbounded fluid. Under such conditions, the system is characterized by the following physical variables: the fluid density  $\rho_f$ , the kinematic fluid viscosity  $\nu$ , the magnitude of the vector of gravitational acceleration  $g = |\mathbf{g}|$ , the particle diameter  $D$ , the particle density  $\rho_p$  and the solid volume fraction  $\Phi_s$ . Dimensional analysis then shows that the problem is determined by three non-dimensional parameters: the aforementioned solid volume fraction  $\Phi_s$ , the density ratio  $\rho_p/\rho_f$  and the Galileo number  $Ga$ . The latter quantity can be written in the form of a Reynolds number, viz.  $Ga = u_g D/\nu$ , with the gravitational velocity scale given by  $u_g = (\rho_p/\rho_f - 1|Dg|)^{1/2}$ . Incidentally, a gravitational time scale can be defined as  $\tau_g = D/u_g$ .

In the present study we have performed direct numerical simulations of two main parameter points (cf. table 1 for the physical parameter values). In both cases the value of  $\Phi_s = 0.005$  was chosen for the global solid volume fraction, i.e. we consider a rather dilute suspension for which, however, the indirect interaction between the particles via the carrier phase can be significant as will be shown. Furthermore, a solid-to-fluid density ratio of  $\rho_p/\rho_f = 1.5$  was selected for both cases; this value corresponds to the value of some plastic materials (such as PVC) in water. Finally, two values of the Galileo number have been simulated, namely  $Ga = 121$  and  $178$ , which is the only physical parameter that has been varied in the present study. These two main simulations are denoted as M121 and M178.

Let us briefly recall the regimes of motion a single isolated particle experiences at the chosen density ratio  $\rho_p/\rho_f = 1.5$ , which are attained asymptotically in time when starting from an initially ambient fluid and a particle at rest, as mapped out by Jenny *et al.* (2004) and Uhlmann & Dušek (2014). For values of the Galileo number below  $Ga_{cr1} \approx 155$  the wake is axi-symmetric and consists of a single toroidal vortex structure attached to the particle, the particle settling steadily on a

straight vertical path. When increasing the Galileo number beyond this value  $Ga_{cr1}$ , the wake becomes oblique (with planar symmetry) and features a pair of thread-like quasi-axial vortices; the motion in this regime is steady and follows a path with a small inclination with respect to the vertical direction, i.e. the particle experiences a finite horizontal drift with a random direction in the horizontal plane. Above  $Ga_{cr2} \approx 185$  the wake becomes time-dependent and hairpin-shaped, exhibiting periodic oscillations around the above mentioned oblique state; the previous symmetry is still maintained and, therefore, the fluctuating particle motion is confined to a plane in space. For values larger than  $Ga_{cr3} \approx 215$  the periodicity and the planar symmetry are lost, and eventually chaotic particle motion with zero average drift in the horizontal plane sets in. The sequence of flow regimes and the corresponding wake structures for isolated particles are illustrated in figure 1. Therefore, the two parameter values (regarding  $Ga$  and  $\rho_p/\rho_f$ ) chosen for the present multi-particle sedimentation simulations correspond to the axi-symmetric wake regime ( $Ga = 121$ ) and to the regime of steady oblique motion ( $Ga = 178$ ) when considering an isolated particle.

The simulations were performed in triply-periodic, cuboidal computational boxes, one set of edges being aligned with the direction of gravity. The Cartesian coordinate system is arranged such that the  $z$ -coordinate points opposite to the direction of gravity, while  $x$  and  $y$  are the remaining coordinates in the horizontal plane. Since such a periodic system does not attain a steady state in the presence of settling spheres, a constant vertical pressure gradient (i.e. a homogeneous body force) was imposed whose integral (over the domain) equals the total submerged weight of the suspended particles. In both cases the domain is elongated in the direction of gravity in order to account for the anisotropic length scales of the particle wakes. The employed domain sizes are shown in table 1. The vertical domain length  $L_z$  is two orders of magnitude larger than the particle diameter, corresponding to  $341D$  and  $170D$  in case M121 and M178, respectively. In each horizontal direction, a linear dimension of  $68D$  (case M121) and  $85D$  (case M178), respectively, was chosen. The adequacy of these box sizes for the representation of the current sedimentation problem will be discussed in § 2.4.

In order to represent the flow field in the vicinity of the particles faithfully, we employ a (uniform) grid width  $\Delta x = \Delta y = \Delta z$  such that a particle diameter is resolved by 15 (24) grid points in case M121 (M178), as shown in table 2. This choice takes into account the increase in Galileo number between these cases, as reflected by the different basic wake regimes of the corresponding isolated particle motion (axi-symmetric toroidal wake versus double-threaded oblique wake). Further discussion of the grid convergence of our results is presented in § 2.3. From the domain size and the grid resolution normalized by the particle diameter, the number of grid nodes of the computational mesh is readily obtained (table 2), amounting to a total of  $1024^2 \times 5120$  ( $2048^2 \times 4096$ ) in case M121 (M178). In our configuration the solid volume fraction is given by the relation  $\Phi_s = N_p(\pi/6)D^3/(L_x L_z L_y)$ , where  $N_p$  is the number of particles in the periodic cell. With the above numbers it turns out that the motion of  $N_p = 15190$  and  $11867$  particles, respectively, is tracked in the two cases (cf. table 2). A visualization of the computational domain and the initial particle positions is shown in figure 2.

Additionally we have performed a set of complementary simulations of the settling of a single particle (denoted as “S121” and “S178” in table 1) with identical density ratio and Galileo number as in the multi-particle cases M121 and M178. These additional simulations were performed in smaller boxes than the main cases, yet at very low solid volume fraction (two orders of magnitude smaller than M121 and M178). Consequently, they will be used as reference data devoid of multi-particle effects in the following discussion.

## 2.3 Validation

The present numerical method and its computer implementation have undergone a wide range of validation tests and benchmarks (cf. Uhlmann, 2004, 2005a,b, 2006, 2008).

In order to determine the required small-scale resolution for the computationally demanding simulations presented herein, we have performed some additional tests. They consisted in grid convergence simulations of the settling of a single mobile particle in a uniform flow (featuring a uniform inflow plane and convective outflow instead of periodicity in the vertical direction).

Reliable reference data from spectral/spectral-element computations with a boundary conforming grid (using a moving grid attached to the particle) is available for this case. This set-up allowed us to benchmark our method with regards to the subtle effects arising when the coupled fluid-particle system undergoes a bifurcation at increasing Galileo number. The proposed benchmark is, therefore, a very stringent test for a non-boundary-conforming numerical method. We have found that a resolution of  $D/\Delta x = 15$  is capable of reproducing the axi-symmetric wake regime (at  $Ga = 144$ ) correctly with a maximum error on the particle velocity of approximately 6%. Turning to the double-threaded wake regime ( $Ga = 178$ ), an increased resolution of  $D/\Delta x = 24$  captures the oblique particle motion faithfully with a comparable quality. Please note that although the (asymptotic) particle motion is steady in the Lagrangian frame of reference in these two regimes, the simulations on a fixed computational mesh are still time-dependent. The details of these validation tests as well as data at supplementary parameter points can be found in [Uhlmann & Dušek \(2014\)](#).

## 2.4 Simulation start-up procedure

The initial particle positions were set randomly. As the Voronoï analysis discussed in § 3.2.1 shows, the initial state determined by the pseudo-random number generator indeed reflects the expected statistics of a random Poisson process.

In order to speed up the computation of the initial transients when the particles accelerate from rest up to values comparable to their terminal velocity, we have combined two strategies: a) simulating first the flow around fixed particles, then releasing them; b) using first a coarser grid, then successively refining it. In particular, we have started with a coarse-grid simulation (using  $D/\Delta x = 7.5$  in case M121 and  $D/\Delta x = 6$  in case M178) of the flow around fixed particles and evolved the simulation in time until a statistically stationary state was reached (covering an interval of  $531\tau_g$  and  $746\tau_g$  in cases M121 and M178, respectively). The relative flow velocity (in the positive  $z$ -direction) was chosen such that the expected average particle drag force approximately balances the submerged weight of the particles, i.e. anticipating the Reynolds number of the freely mobile particles to be equal to the one of the flow around the fixed ones ( $Re = 142$  and  $231$  in cases M121 and M178, respectively). In order to maintain the relative motion, a homogeneous body force in the vertical component of the fluid momentum equation was added, similar to the case of settling spheres.

After the initial coarse simulation, the final flow field was interpolated linearly upon a twice finer grid ( $D/\Delta x = 15$  in case M121 and  $D/\Delta x = 12$  in case M178) and the simulation was continued with the particles fixed for another  $142\tau_g$  ( $283\tau_g$ ) in case M121 (M178). In the lower Galileo number simulation M121 the particles were then released, and the simulation was run for  $3567\tau_g$ . In the higher Galileo number case M178 the final flow field was once more refined to the final resolution  $D/\Delta x = 24$  and the simulation was run for another  $54\tau_g$  with the particles fixed in space. Subsequently the particles in case M178 were released and an interval of  $1672\tau_g$  at the final resolution was simulated considering mobile particles. Henceforth, the instant in time when particles were released is arbitrarily set to zero.

At this point let us quickly mention the computational resources spent for the present computations. The simulation M121 was run on 640 processor cores on the IBM System x iDataPlex system at LRZ München (requiring  $2.3 \cdot 10^6$  CPU core hours) and for case M178 we used 8192 processor cores of the Blue Gene/p system at JSC Jülich ( $2.5 \cdot 10^7$  CPU core hours).

## 2.5 Evaluation of the box-size

Figures 3 and 4 show the two-point correlation function of fluid velocity fluctuations for both cases just prior to the release of the particles. Recall that this corresponds to the flow at sphere Reynolds numbers  $Re = 142$  and  $231$ , respectively, around an array of randomly positioned, fixed spheres. Therefore, the particle wakes are already fully developed and in a statistically stationary state at this point in time. It can be seen from the figures that in the horizontal directions all velocity signals are essentially decorrelated for separations larger than 10 particle diameters, a

distance which is much smaller than the horizontal domain size. Concerning vertical separations, the graphs show that the vertical velocity component is not fully decorrelated at separations of half the box height (while the horizontal velocity component does decorrelate). The correlation coefficient  $R_{ww}$  measures 0.07 (0.14) in case M121 (M178) at the largest separation along the  $z$ -coordinate. This is obviously owed to the strong anisotropy of the particle wakes. It should be kept in mind, that the velocity field of the flow around the fixed particles contains a three-dimensional time-average contribution which affects the correlation lengths. We can conclude this discussion by stating that even larger (axial) domain extensions are necessary if full decorrelation of the flow around dilute random arrays of fixed spheres is desired. However, preliminary coarse grid simulations (at  $Re = 230$ ) have shown that even an extended axial domain size of  $L_z = 680D$  does not warrant full decorrelation.

## 2.6 Notation

Before turning to the results, let us fix the basic notation followed throughout the present text. The spatial domain occupied by the two phases is given by  $\Omega = \Omega_f \cup \Omega_p$ , where  $\Omega_f$  and  $\Omega_p$  are the domains occupied by the fluid and the particles, respectively. Velocity vectors and their components corresponding to the fluid and the particle phases are distinguished by subscripts “f” and “p” respectively, as in  $\mathbf{u}_f = (u_f, v_f, w_f)^T$  and  $\mathbf{u}_p = (u_p, v_p, w_p)^T$ . Similarly, the  $i$ th particle’s position vector is denoted as  $\mathbf{x}_p^{(i)} = (x_p^{(i)}, y_p^{(i)}, z_p^{(i)})^T$ , the vector of angular particle velocity as  $\boldsymbol{\omega}_p^{(i)} = (\omega_{p,x}^{(i)}, \omega_{p,y}^{(i)}, \omega_{p,z}^{(i)})^T$  and the hydrodynamic force exerted by the fluid on the  $i$ th particle as  $\mathbf{f}_p^{(i)} = (f_{p,x}^{(i)}, f_{p,y}^{(i)}, f_{p,z}^{(i)})^T$ .

The fluctuations of the velocities of each phase are defined with respect to the instantaneous phase average, i.e.  $\mathbf{u}'_f(\mathbf{x}, t) = \mathbf{u}_f(\mathbf{x}, t) - \langle \mathbf{u}_f \rangle_{\Omega_f}(t)$ , and  $\mathbf{u}'_p(i, t) = \mathbf{u}_p^{(i)}(t) - \langle \mathbf{u}_p^{(i)} \rangle_p(t)$ , where the precise definitions of the averaging operators over the particle ensemble,  $\langle \rangle_p$ , and over the volume occupied by the fluid,  $\langle \rangle_{\Omega_f}$ , are given in appendix A. The fluctuations of the angular particle velocity are analogously defined.

## 3 Results

### 3.1 Temporal evolution of the system

Here we are concerned with the general evolution of the particulate flow system starting with the moment when the particles are released. Note that the flow field around the fixed particles is already fully-developed at this time (as explained in § 2.4), featuring an average particle Reynolds number commensurate with the terminal settling velocity of isolated spheres at the same Galileo number. Therefore, in the absence of multi-particle effects, the released spheres are expected to settle at the same Reynolds number as was set for the flow around the corresponding fixed spheres.

Let us first consider the average settling velocity. For this purpose we define (at time  $t$ ) the  $i$ th particle’s velocity relative to the fluid-phase-averaged velocity as follows

$$\mathbf{u}_{pr}(i, t) = \mathbf{u}_p^{(i)}(t) - \langle \mathbf{u}_f \rangle_{\Omega_f}(t). \quad (1)$$

The standard definition of the average settling velocity then corresponds to the average over all particles (at a given time) of the vertical component of (1), viz.

$$w_s(t) = \langle w_{pr}(i, t) \rangle_p. \quad (2)$$

Figure 5 shows the temporal evolution of the average settling velocity according to relation (2), normalized with a viscous velocity scale,  $w_s D / \nu$ . It can be seen that the multi-particle ensemble in case M121 settles at approximately the same rate as the corresponding isolated particle, the curve being essentially flat with  $Re = |\langle w_s \rangle_t| D / \nu = 141.6$  (cf. table 1). The collective effect of many particles at solid volume fraction  $\Phi_s = 0.005$  apparently does not lead to a modification of the average settling velocity at  $Ga = 121$  (at a density ratio of 1.5). Conversely, for case M178

figure 5 shows an initial increase of the magnitude of the average settling velocity; the curve then levels off and fluctuates around a value of  $Re = 260.6$ . Different time scales can be distinguished in the signal of the average settling velocity in case M178 in the developed regime, the largest of which being of the order of several hundred  $\tau_g$ . The collective enhancement of the average settling velocity (as defined in 2) in case M178 measures approximately 12% when compared to the value of an isolated particle in case S178 (cf. table 1). A difference of this amplitude is obviously significant in many applications and merits a detailed investigation. Note that the only physical difference between cases M121 and M178 is the value of the Galileo number. As we will see in the following, the particle phase is forming agglomerations in case M178 (cf. § 3.2, where the properties of the spatial particle distribution will be discussed), which lead to an increase in  $|w_s|$  (cf. § 3.3.2).

In figure 6 the time evolution of the intensities of velocity fluctuations of both phases are shown (cf. definition given in § 2.6). In case M121 a short initial transient is visible after which the vertical components of both phases exhibit slow fluctuations with a time scale of the order of one thousand gravitational time units. On the other hand, the curves of case M178 again settle into an asymptotic behavior after approximately  $200\tau_g$  after which oscillations with comparably shorter period ensue. While the scaling of the amplitude of these and other (globally averaged) signals will be discussed in more detail in § 3.3, at present we are only concerned with the definition of the time interval over which temporal statistics are computed. For consistency between the two flow cases, we have chosen to consider the flow as fully-developed for  $t \geq 200\tau_g$  in both instances. Therefore, the time interval over which the statistically stationary state is observed corresponds to  $T_{obs} = 2967\tau_g$  ( $1472\tau_g$ ) in case M121 (M178). %

## 3.2 Spatial structure of the dispersed phase

Figure 7 shows a visualization of instantaneous particle positions in case M121 with the view directed along the vertical axis. Comparing the random initial positions (figure 7a) to those at some instant when the system is in a statistically stationary state (figure 7b) reveals no significant difference. The corresponding visualization for case M178 is shown in figure 8. It is clearly observable that the particle distribution after the initial transient deviates significantly from the initial distribution. Localized regions in the projection upon the horizontal plane with a high number density of particles alternate with regions practically devoid of particles. It should be noted that the box size (in multiples of the particle diameter) and, consequently, the number of particles in case M121 is significantly larger than in case M178. Therefore, the illustrations of the initial random state (figure 7a vs. 8a) differ somewhat.

Hereafter, regions with high particle concentration are loosely referred to as “clusters” and regions with low particle concentration as “voids”, where the definition of high- and low- particle concentration will be made more precise later in this section. Seen from this vertical view the particles in case M178 appear to form structures which are elongated in the vertical direction. Close inspection reveals that the clusters and the voids extend throughout the entire height of the computational domain. The characteristic size of the clusters in the horizontal direction, however, is much smaller than the computational domain. The present visual detection of clusters is in line with previous findings where a similar “columnar particle accumulation” was reported at similar parameter values (Kajishima, 2004). Time sequences of particle position graphs show that these structures persist over long time intervals. We will return to this point shortly.

### 3.2.1 Voronoï analysis

In the following we quantify the tendency of the particles to form clusters by performing a Voronoï analysis of the particle positions. A number of techniques have been established for the characterization of the spatial structure of the dispersed phase: box counting (Fessler *et al.*, 1994), pair correlation function estimation (Sundaram & Collins, 1997), genuine clustering detection algorithms (Wylie & Koch, 2000; Melheim, 2005), nearest-neighbor statistics (Kajishima, 2004) and Voronoï tessellation (Monchaux *et al.*, 2010b, 2012). The latter technique has the advantage of



providing a rich set of geometrical information without the need for choosing any length scale a priori, while at the same time being computationally efficient.

The term Voronoï tessellation corresponds to a decomposition of space into an ensemble of cells  $\mathcal{V}_i$ , each of which being associated to one particle, i.e. with  $1 \leq i \leq N_p$ . The Voronoï cells possess the property that all points inside the  $i$ th cell are located closer to the centroid of the  $i$ th particle than to any other particle (Okabe *et al.*, 1992). Examples of Voronoï diagrams in two- and three space dimensions are shown in figure 9. The cells are periodically extended such as to fill the space (figure 9a). Note that the Voronoï analysis performed here is three-dimensional. From the tessellation one can determine the volume of each cell, henceforth denoted as  $V_i$ , which can be related to the inverse of the local particle concentration, i.e. Voronoï cells with small (large) volume indicate regions with high (low) particle concentration. The Voronoï cell volumes analyzed in the following are normalized such that the mean value measures unity, which removes the dependence upon the particle number density (Ferenc & Neda, 2007).

Figures 10a and 11a depict the p.d.f. of the normalized Voronoï volumes for both flow cases at different times during the course of the simulations. Except for the initial state, the tessellations are performed at several instants covering short time intervals of length of less than  $30\tau_g$  and then averaged to increase the number of samples. It can be seen that the initial state (which was determined pseudo-randomly) is well represented by a Gamma distribution which corresponds to a random Poisson process (Ferenc & Neda, 2007). In case M121 (figure 10a) the p.d.f. of the Voronoï cell volumes tends to a shape which is narrower than the initial random particle distribution. This indicates that the particle distribution in case M121 becomes more ordered than randomly distributed particles. Conversely, in case M178 (figure 11a), the curves broaden once particles are released. In the statistically stationary regime they exhibit tails with significantly higher probability of finding cells with very large or very small volumes than in the random case, indicating that cluster (and void) formation takes place.

Monchaux *et al.* (2010a) have used the standard deviation of the p.d.f. of the normalized Voronoï cell volumes in order to quantify the particles' tendency to cluster. Figure 12 depicts this quantity as a function of time for our two cases. As can be seen, the standard deviation in case M121 decreases after particles have been released to settle freely and quickly reaches a state where it fluctuates lightly around a value of 0.345. By way of comparison, the value corresponding to the random arrangement measures 0.411 (note that this value is slightly smaller than the value of 0.447 computed by Ferenc & Neda, 2007, due to the finite size of the present particles). Contrarily, the standard deviation in case M178 increases with time and reaches a statistically steady value of 0.616, exhibiting somewhat larger temporal fluctuations. From the figure it is clearly observable that the transient time for the particles to reach a statistically steady state is considerably longer in case M178 than in case M121, in line with the observed transients of particle and fluid velocity fluctuations discussed in § 3.1.

We have further analyzed the particle distribution by computing the aspect ratio of each Voronoï cell, defined as the ratio of its largest horizontal extension  $l_H(\mathcal{V}_i)$  to its largest vertical extension  $l_V(\mathcal{V}_i)$ , viz.

$$A_i = l_H(\mathcal{V}_i)/l_V(\mathcal{V}_i) \quad \forall i = 1 \dots N_p. \quad (3)$$

The so-defined aspect ratio provides a measure of the anisotropy of the Voronoï cells. Figures 10b and 11b show the data for both flow cases again at different times during the simulation. In case M121 no significant deviation from the p.d.f. of the randomly distributed particles is observed. This means that the tendency towards a more ordered state (observed in conjunction with the data for the Voronoï cell volume, cf. figure 10a) is not accompanied by a change in the geometrical aspect ratio at the lower Galileo number. In contrast, in case M178 an appreciable difference is observed in the statistically stationary state. Finding Voronoï cells with large values of  $A_i$  is more probable than in the case of randomly distributed particles. This is an indication that the majority of the Voronoï cells are squeezed (stretched) in the vertical (horizontal) direction. The result is consistent with the fact that the particles in case M178 have a tendency to be aligned in the vertical direction, as already visually noted for one snapshot in figure 8b.

The Voronoï cell volume data can be used to define an intrinsic definition of cluster regions and

voids by determining the intersection points between the p.d.f. of the DNS data and that of the random distribution: particles whose Voronoï cell volume is smaller than the lower intersection point  $V^c$  are considered to be located in a cluster and those whose Voronoï cell volume is larger than the upper intersection point  $V^v$  are attributed to void regions (Monchaux *et al.*, 2010a). By tracking the particle positions in time, we can compute statistics on the temporal behavior with respect to clustering. It turns out that in case M178 the mean residence time of the particles in clusters (voids) measures  $24.9\tau_g$  ( $87.7\tau_g$ ). This indicates, that once the particles enter clusters or void regions they remain trapped therein for relatively long times, with a bias towards voids. It should be noted, however, that the Voronoï tessellation attributes rather large cell volumes to particles located on the periphery of clusters. We have checked that with the above definition, at any given time in the statistically stationary regime of case M178 approximately 30% of the particles reside in clusters and 15% in void regions, with little temporal fluctuations.

Since each Voronoï cell can be uniquely assigned to a single particle, the derived quantities can be tracked in time. This allows us to study the behavior of these geometrical quantities in a Lagrangian manner. The auto-correlation function related to a quantity  $Q_V(t)$  is defined as

$$R_{Q_V Q_V}(\tau_{sep}) = \frac{\langle Q'_V(t) Q'_V(t + \tau_{sep}) \rangle_{p,t}}{\langle Q'_V(t) Q'_V(t) \rangle_{p,t}}, \quad (4)$$

where  $Q'_V(t) = Q_V(t) - \langle Q_V \rangle_{p,t}$  is the fluctuation with respect to the mean over the particle ensemble and time (cf. appendix A).

The auto-correlation corresponding to the Voronoï cell volume is shown in figure 13. It can be observed that the correlation time is somewhat larger in the clustering case M178 than in the counterpart M121 where no clustering takes place. The corresponding integral time scale measures  $43.7\tau_g$  ( $73.7\tau_g$ ) in case M121 (M178). The Taylor micro-scale, however, is similar in both cases:  $15.8\tau_g$  (case M121),  $13.7\tau_g$  (case M178). Regarding the Voronoï cell aspect ratio (included in the same figure) it exhibits a similar behavior in both flow cases, featuring a considerably faster decorrelation than the cell volume. The corresponding integral time scale measures  $17.2\tau_g$  ( $14.2\tau_g$ ) in case M121 (M178). Note that the Voronoï cell aspect ratio is a geometrical property of the shape of the cells; therefore, it may be significantly modified while the particle positions dynamically rearrange without necessarily changing the volume of the corresponding cells.

### 3.2.2 Conditionally averaged particle concentration

From the Voronoï analysis of § 3.2.1 we are able to determine whether the particles tend to form agglomerations as a whole – which was seen to be the case in simulation M178. In this section we study the *local* particle distribution in the vicinity of a test particle. This kind of analysis will provide more insight into the micro-structure of the dispersed phase. For this purpose we have performed particle-conditioned averaging of the locations of the remaining particles. Since the conditioned field is axi-symmetric (the axis coinciding with the vertical direction), the significant data is defined in a plane including the vertical direction. Using the computational grid of the simulations we first define for each grid cell a solid phase indicator function. The origin of this field is then shifted to each particle location (taking into account periodic wrap-around) and added up; this process is then repeated (additively) for a number of 16816 (26180) particle snapshots in case M121 (M178) and dividing by the number of samples, yielding a field with values in the interval  $[0,1]$  (Kidanemariam *et al.*, 2013). The result, which will be denoted by  $\phi_s^{cond}(\tilde{r}, \tilde{z})$ , can be interpreted as the probability that a point with coordinates  $(\tilde{r}, \tilde{z})$  – with respect to the center of a test particle – is located inside the solid phase domain  $\Omega_p$  (cf. appendix A.2 for a precise definition). When normalizing this quantity with the global solid volume fraction  $\Phi_s$ , the result is closely related to the pairwise distribution function (Sundaram & Collins, 1997; Shotorban & Balachandar, 2006; Sardina *et al.*, 2012). For visual clarity the following visualizations are shown (redundantly) for the half plane instead of the fundamental quadrant.

Figures 14 and 15 show the two dimensional maps of  $\phi_s^{cond}/\Phi_s$  for both flow cases. As can be clearly seen, on a macroscopic level the dispersed phase in case M121 (figure 14a) does not show any signs of accumulation, and particles appear to be randomly distributed. Only at close proximity of

the reference particle can we observe a non-trivial structure (figure 14b): the probability of finding another particle is significantly larger than the global average on the vertical axis at a distance around one particle diameter; it is below average principally at small horizontal separations from the test particle and over a range of angles with respect to the horizontal.

In case M178 (figure 15a), the distribution of the conditioned solid volume fraction clearly exhibits a strongly anisotropic spatial structure even at the macroscopic level, featuring high values of the local concentration in form of a streamwise elongated stripe around the vertical axis. As can be seen, the region of high local particle density extends throughout the entire height of the computational domain. This is in line with the observed clustering in columnar structures. The micro-structure in case M178 (figure 15b) also differs from the lower Galileo case M121: in particular, a small region with larger than average solid volume fraction is found at horizontal distances around  $1.5D$ .

The spatial variation of the conditioned solid volume fraction can be more conveniently examined in a quantitative fashion by considering vertical and horizontal profiles through the center of the reference particle, as shown in figure 16. Let us first consider the horizontal direction (figure 16a). In case M121 the normalized solid volume fraction increases slowly and reaches unity at a horizontal distance of approximately  $\tilde{r} = 2.5D$  from the surface of the reference particle; beyond that distance the solid volume fraction remains close to unity. In case M178, on the other hand, a faster increase with horizontal distance is observed, crossing unity at  $\tilde{r} \approx D$ , leading up to a maximum value  $\phi_s^{cond}/\Phi_s \approx 2$  located at  $\tilde{r} \approx 1.5D$ , then levelling back off towards unity at a rate approximately proportional to  $\tilde{r}^{-0.65}$ . The lateral region which is depleted of particles is therefore much smaller in the clustering case M178 than in case M121.

Turning to the vertical direction (figure 16b), we observe nearly identical conditioned solid volume fraction values in both cases for small distances from the test particle (up to  $1.5D$ ). Beyond that point, the curve corresponding to case M121 decreases and reaches unity from above at a distance of roughly  $8D$ . In case M178, however, the probability to find a particle keeps increasing up to a vertical distance of approximately  $3D$ , beyond which point it slowly decays, not reaching unity within the present domain size. Thus, the macroscopic behavior of the particle-conditioned solid volume fraction along the vertical axis directly reflects the observed clustering of particles in case M178. The micro-structure, however, is remarkably similar in both cases. It appears that a “robust” mechanism is at play, which does not strongly depend upon the Galileo number over the presently investigated range.

At lower Reynolds number (up to a value of 10) information on the micro-structure of the dispersed phase is available for rising bubbles from the experimental measurements of [Cartellier \*et al.\* \(2009\)](#) and for sedimenting suspensions from the numerical simulations of [Yin & Koch \(2008\)](#). In the former study, a deficit of close vertically-aligned bubble pairs was observed with a decreasing extent when the bubble concentration (void fraction) was increased. In the case of [Yin & Koch \(2008\)](#) the solid volume fraction was kept constant at a value of 0.01, while the particle Reynolds number was varied (in the range of 1 to 10). The authors found that the extent of the deficit of vertical pairs grows with the Reynolds number and that an excess of horizontal pairs occurs at  $Re = 10$ ; both observations were attributed to wake-induced “drafting-kissing-tumbling” of particle pairs (cf. [Fortes \*et al.\*, 1987](#); [Wu & Manasseh, 1998](#)). The micro-structure observed by [Yin & Koch \(2008\)](#) is therefore qualitatively different from the present cases. At the time being, however, the gap in parameter space with respect to those lower Reynolds number suspensions appears too large to be bridged by straightforward arguments.

### 3.3 Particle motion

In order to analyze the motion of finite-size particles in detail, it is useful to work with relative velocities between the two phases. This immediately leads to the question of the most adequate definition of a fluid velocity with respect to which the relative particle motion should be computed. Therefore, before turning to the actual statistical results, we first provide a definition of the fluid velocity in the vicinity of a finite-size particle. We believe that this step is vital to an understanding of the dynamics of finite-size particles where no straightforward measure of the fluid velocity

relevant to a given particle exists.

### 3.3.1 Fluid velocity seen by the particles

There have been various approaches to defining a fluid velocity “seen” by the particles. [Bagchi & Balachandar \(2003\)](#) investigated the effect of turbulence on the drag and lift of a single particle, performing DNS of homogeneous-isotropic turbulence swept past a fixed sphere. The fluid velocity “seen” by the particle was alternatively defined either (i) as the fluid velocity at the position of the particle in an (otherwise identical) particle-free simulation, or (ii) as the fluid velocity averaged over a spherical volume centered at the particle centroid in the corresponding particle-free simulation. [Merle \*et al.\* \(2005\)](#) investigated the forces acting on a bubble in a turbulent pipe flow. Taylor’s hypothesis was invoked in order to define the fluid velocity “seen” by the bubble without recurring to a particle-free companion simulation. [Lucci \*et al.\* \(2010\)](#) investigated the modification of homogeneous-isotropic turbulence by particles of size comparable to the Taylor micro scale (in the absence of gravity). They proposed two definitions of the fluid velocity “seen” by the particles: (i) the fluid velocity at a distance (comparable to the Taylor micro-scale) away from the particle surface, taken in the direction of the instantaneous particle velocity vector, and (ii) essentially the same definition, but averaging over a small spherical cap. In both cases, the use of the directional information from the instantaneous particle velocity (in an inertial frame) is questionable, as noted by [Kidānemariam \*et al.\* \(2013\)](#).

Here, we use the definition proposed by [Kidānemariam \*et al.\* \(2013\)](#), where the relevant fluid velocity in the vicinity of a particle is approximated by the average of the fluid velocity over the surface  $\mathcal{S}$  of a sphere with radius  $R_S$  centered at the particle’s center location; this velocity corresponding to the  $i$ th particle at time  $t$  will henceforth be denoted by  $\mathbf{u}_f^S(i, t, R_S)$ . Note that [Cisse \*et al.\* \(2013\)](#) have recently proposed a similar definition based upon the mass flux entering a spherical shell. We presently choose the same averaging radius as [Kidānemariam \*et al.\* \(2013\)](#), i.e. we set  $R_S = 1.5D$ . This choice essentially assures on the one hand that the particle’s own boundary layer is not significantly affecting the resulting fluid velocity measure while at the same time  $R_S$  is sufficiently small for the result to be directly relevant to the generation of the hydrodynamic force (and torque) acting on the respective particle. The reader is referred to that reference for a discussion of the chosen value of the averaging radius. From now on the symbol “ $R_S$ ” will be dropped from the list of arguments of the quantity  $\mathbf{u}_f^S$  for the sake of conciseness.

In order to characterize the effect of particle-conditioned averaging over a spherical surface, we have compared the statistics of the resulting velocity values  $\mathbf{u}_f^S$  to those of the entire (unconditioned) fluid velocity field  $\mathbf{u}_f$ . Information related to the first and second moments of the vertical component are listed in table 3. It can be seen that in both flow cases the mean value of the particle-conditioned vertical fluid velocity is smaller than the unconditioned one. However, in case M121 the difference  $\langle w_f^S \rangle_{p,t} - \langle w_f \rangle_{\Omega_f,t}$  only amounts to approximately 3% of the absolute value of the conventional settling velocity  $|\langle w_s \rangle_t|$  (cf. equation 2), while the (absolute value of the) difference is larger than 11% in case M178. Consequently, it can be said that the particles in the higher Galileo number case M178 are surrounded (on average) by fluid with a significantly smaller vertical velocity than the box-averaged value, i.e. they are located inside regions with a downward fluid motion (as compared to the globally-averaged fluid velocity). Incidentally, let us mention that in both flow cases the standard deviation of the vertical component of the particle-conditioned fluid velocity is significantly smaller than the unconditioned counterpart. This result is believed to reflect the fact that averaging over the surface of a sphere with diameter  $3D$  acts like a spatial filter which tends to suppress small-scale fluctuations. However, the shapes of the normalized p.d.f.s of the particle-conditioned fluid velocity field are very similar to those of the unconditioned field (figures omitted).

With the chosen definition of the relevant fluid velocity in the vicinity of the particles, we can now define an instantaneous relative velocity based upon a local reference value, viz.

$$\mathbf{u}_{pr}^S(i, t) = \mathbf{u}_p^{(i)}(t) - \mathbf{u}_f^S(i, t) \quad \forall i = 1 \dots N_p. \quad (5)$$

The difference between this definition and the standard one given in (1) is that in (5) both values

– the particle and the fluid velocity – are evaluated locally. It can therefore be expected that the definition given in (5) provides a better representation of the local flow conditions which affect the particle motion. The mean settling velocity with respect to each particle’s surrounding fluid region is then simply defined by applying an average over the particle ensemble to the vertical component of (5), viz.

$$w_s^S(t) = \langle w_{pr}^S(i, t) \rangle_p. \quad (6)$$

In the limit of the averaging radius  $R_S$  tending to infinity the particle-conditioned settling velocity according to definition (6) tends to the conventional settling velocity based on the globally averaged fluid velocity (2). For finite values of the shell radius  $R_S$ , the difference between the present definition of the average settling velocity (6) and the conventional definition (2) is, therefore, entirely due to the two different definitions of the fluid velocity, reflecting the fact that particles do not sample the flow field uniformly.

### 3.3.2 Average settling velocity

Let us return to figure 5 which shows the average settling velocity (according to the two alternative definitions) as a function of time. Recall that in case M121 (where no clustering occurs) the collective settling velocity defined with respect to the box-averaged fluid velocity  $w_s$  (cf. equation 2) is practically identical to the value of an isolated particle, whereas in case M178 (in the presence of clustering) the collective effect manifests itself through a strongly enhanced absolute value of  $w_s$ . When using the average settling velocity with respect to the local fluid velocity  $w_s^S$  (defined in 6), the absolute value of the settling velocity is correspondingly reduced. More specifically, in case M121 the average settling velocity with respect to the fluid in each particle’s vicinity remains close to the settling velocity of an isolated particle (since  $\langle w_f^S \rangle_{p,t}$  is not too different from  $\langle w_f \rangle_{\Omega_f,t}$ , as seen in table 3). In case M178, however, the significant difference in the definition of the fluid velocity brings the settling velocity  $w_s^S$  close to the single particle reference value (the absolute value of the former is upon time-average approximately 3.3% smaller than the latter). % % It appears that the particles in case M178 are (on average) locally moving at a vertical relative velocity which is similar to the value for a single particle, albeit slightly smaller. Our results therefore suggest that the observed enhanced global settling rate in case M178 is a direct consequence of particles being located preferentially in regions where the fluid velocity fluctuation (with respect to the box-average) is negative.

As the previous analysis shows, in the clustering case M178 it makes a large difference whether the relative velocity is computed with respect to the global average of the fluid velocity or whether it is evaluated locally. This also implies that in the respective flow case the spatial variability of the settling velocity is large. Next, we would like to establish a direct link between the vertical particle velocity and the (instantaneous) regions where the particle concentration is higher/lower than the average. For this purpose we have computed the joint p.d.f. of the fluctuations of the particle settling velocity (defined with respect to the box-averaged fluid velocity, cf. equation 1) and the fluctuation of the Voronoï cell volume associated to the respective particle at the respective time, as shown in figure 17. It can be seen that the two quantities are not significantly correlated in case M121 (the correlation coefficient measures 0.002). In the clustering case M178, on the other hand, one can clearly observe a positive correlation with a correlation coefficient of 0.347, i.e. small Voronoï cells tend to correspond to smaller-than-average relative vertical velocities (equivalent to faster settling particles) and vice versa. This result confirms that in case M178 the fast settling particles are indeed – statistically speaking – located in agglomeration regions, while the slowly settling particles are found with a higher probability in void regions. Note that the average deviation of the settling velocity from the global mean is not linearly related to the Voronoï cell volumes, as can be seen from the conditional mean  $\langle w'_{pr} | V'_i \rangle$  included in figure 17(b). An illustration is provided in figure 18 which shows the particle positions at one instant (viewed from the top) colored according to their settling velocity value  $w_{pr}(i, t)$ . The correlation between agglomerations (voids) and smaller (larger) than average vertical relative velocity values is evident in case M178. In case M121, on the other hand, such a correlation is not clearly visible; instead, fast and slowly settling particles appear to be much less clearly segregated in the horizontal direction.

In order to demonstrate the spatial correspondence between fast settling clusters and downward fluid motion (with respect to the box-average), we compute the instantaneous vertical average of the vertical component of the fluid velocity (cf. equation 16); its fluctuation is defined as follows:  $\hat{w}'_f(x, y, t) = \langle w_f(\mathbf{x}, t) \rangle_z - \langle w_f(\mathbf{x}, t) \rangle_{\Omega_f}$ . Figure 19 shows this quantity (normalized by the box-averaged value) at the same instant as the particle data shown in figure 18. In case M178 we indeed observe regions of significantly smaller-than-average fluid velocities at those locations where notable particle agglomerations occur and vice versa for voids. In case M121, on the contrary, the vertically-averaged fluid velocity  $\hat{w}'_f$  is of significantly smaller amplitude and it is more evenly distributed in space. A representative illustration of the flow field is rendered in figure 20 where iso-surfaces of the vertical fluid velocity fluctuations  $w'_f$  in case M178 are shown at values of  $\pm 0.4u_g$ . Both negative and positive values correspond to a number of tube-like vertical structures traversing essentially the whole domain. In case M121, on the contrary, where the amplitude of the fluctuations is much smaller (cf. figure 6a), these values are practically not encountered (figure omitted). The shape of the vortical structures in the near-field of the particles in case M178 can be seen in figure 21, where again the criterion of Jeong & Hussain (1995) has been used on an instantaneous flow field. The figure shows a sub-volume of the domain which includes part of one strong downward current (indicated by the large tube-like structure included therein). In the cluster regions, the particle wakes feature complex tangles of vortices extending from particle to particle and beyond. In more quiescent regions, particle wakes are found to be much closer to the double-threaded state of an isolated sphere at the same Galileo number (cf. regime II in figure 1). The corresponding visualization in case M121 (presently omitted) shows attached toroidal vortex rings for most particles, similar to those found in regime I of an isolated particle (cf. figure 1).

Next we wish to analyze the spatial distribution of the settling velocity. For this purpose we perform particle-conditioned averaging of this quantity, which is analogous to computing the particle-conditioned solid volume fraction discussed in § 3.2.2 (cf. figures 14 and 15). The result of applying the particle-conditioned averaging operator (22) to the settling velocity  $w_{pr}(i, t)$  will henceforth be denoted as  $w_{pr}^{cond}(\tilde{r}, \tilde{z})$ . A map of this quantity is shown in figure 22. Note that the quantity  $w_{pr}(i, t)$  is not invariant with respect to an interchange of the indices of the two particles making up any given pair. As a consequence, the map of the particle-conditioned average settling velocity  $w_{pr}^{cond}(\tilde{r}, \tilde{z})$  does not possess a symmetry with respect to the horizontal axis (i.e. the average settling velocity is not necessarily the same for a leading and for a trailing particle); due to horizontal homogeneity; it is, however, still symmetric with respect to the vertical axis passing through the test particle. The map in figure 22 shows that in case M121 trailing particles are indeed settling faster (i.e. their settling velocity is lower) than the average. However, this effect is limited to a compact region in the wake of the test particle. In case M178, on the other hand, the particle-conditioned settling velocity is significantly below the average value (i.e. the settling rate is increased) over long distances in the wake of the test particle, while it is slightly larger than the average (decreased settling rate) at lateral distances  $\tilde{r}$  of approximately 10 particle diameters from the test particle (roughly independent of the vertical distance  $\tilde{z}$ ). A direct comparison of the conditionally-averaged settling velocity in the two simulations is shown in figure 23, where the variation along the vertical axis and along a horizontal axis passing through the test particle is plotted. At small positive vertical distances  $\tilde{z}$  from the test particle (i.e. focusing on closely trailing particles in figure 23a), the spatial variation of the conditioned settling velocity is roughly similar in both flow cases, featuring a steep increase of the settling velocity with  $\tilde{z}$ . Note that the minimum close to the rear of the test particle measures approximately 1.3 times the globally-averaged settling velocity. For larger distances on the vertical axis ( $\tilde{z} \gtrsim 4D$ ), however, the conditional settling velocity in case M178 increases at a much smaller rate than in case M121 (in both cases the asymptotic value -1 is approached exponentially for  $\tilde{z} \gtrsim 15D$ ). Regarding leading particles (i.e. negative values of  $\tilde{z}$  in figure 23a), it is found that they are likewise settling faster (on average) than the global average at any distance in case M178. In case M121, vertically-aligned leading particles are also settling somewhat faster, but only within a distance of a few diameters from the test particle. Turning to horizontal distances (figure 23b), it is found that particles in case M121 which are located within approximately  $5D$  from the test particle settle on average at a smaller speed than the global average. On the contrary, in case M178 slower settling (i.e.

$w_{pr}^{cond}/|\langle w_{pr} \rangle_{p,t}| > -1$ ) is found only for horizontal distances larger than approximately  $5D$ , with a mild peak of  $w_{pr}^{cond}$  at  $\tilde{r} \approx 8D$ .

In conclusion our analysis of the particle-conditioned settling velocity has confirmed that clustering in the higher-Galileo case M178 leads to a patterning of the vertical particle motion which is distinct from the non-clustering case M121, the main feature in the former case being a long-range effect in the vertical direction. The length scales which can be extracted from the particle-conditioned analysis of the settling velocity provide one way of characterizing the geometry of the clusters themselves.

### 3.3.3 Fluctuating quantities

Let us return to the fluctuations of the translational particle velocity. The rms value of the fluctuations,  $\langle u'_{p,\alpha} u'_{p,\alpha} \rangle_p^{1/2}$  (with  $u'_{p,\alpha}$  defined with respect to the instantaneous average over all particles, cf. definition in § 2.6), is shown in figure 6b, which has already been briefly discussed in § 3.1. Recall that asymptotically an isolated particle in case S121 (same density ratio and Galileo number as case M121) settles with a constant velocity along a vertical path, while an isolated particle in case S178 (corresponding to M178 in terms of  $\rho_p/\rho_f$ ,  $Ga$ ) settles steadily along an oblique path in a random horizontal direction. Therefore, ensemble averaging over many realizations of isolated particles in case S121 would produce fluctuating particle velocity rms values equal to zero; in case S178 (due to the randomness of the horizontal orientation) one would obtain an rms value in any fixed horizontal direction which is different from zero. In particular, one would obtain (e.g. considering the  $x$ -direction):

$$\frac{\langle u'_p u'_p \rangle_p^{1/2}}{w_s} = \frac{u_{pH}}{u_{pV}} \frac{1}{\sqrt{2}}, \quad (7)$$

where  $u_{pH}$  and  $u_{pV}$  are the absolute values of the particle velocity in the horizontal plane and along the vertical, respectively, obtained from the simulation of an isolated particle. The value of the quantity given in (7) for an ensemble of cases S178 is 0.065 (Uhlmann & Dušek, 2014). In the present multi-particle case M178, the corresponding time-averaged value over the observation interval, i.e.  $\langle u'_p u'_p \rangle_{p,t}^{1/2}/w_s$ , is much larger, measuring 0.11. This comparison shows that the velocity fluctuation amplitude of the particle ensemble in case M178 cannot be satisfactorily accounted for by means of a simple superposition of isolated particles settling in an undisturbed manner. This is the more true when considering that such superposition yields a zero fluctuation amplitude of the vertical particle velocity component. Next we will decompose the particle velocity in order to separate from the fluctuations those contributions which are due to the motion of the fluid surrounding the particles.

Using our definition of the fluid velocity seen by a particle,  $\mathbf{u}_f^S$  (cf. § 3.3.1), and of the relative velocity between the particle and the surrounding fluid,  $\mathbf{u}_{pr}^S$  (defined in equation 5), the variance of the particle velocity component in the direction  $x_\alpha$  can be decomposed as follows:

$$\langle u'_{p,\alpha} u'_{p,\alpha} \rangle_p = \langle u_{pr,\alpha}^{S'} u_{pr,\alpha}^{S'} \rangle_p + \langle u_{f,\alpha}^{S'} u_{f,\alpha}^{S'} \rangle_p + 2\langle u_{pr,\alpha}^{S'} u_{f,\alpha}^{S'} \rangle_p, \quad \forall \alpha = 1, 2, 3, \quad (8)$$

where all fluctuations are defined with respect to the instantaneous average over the particle ensemble, viz.

$$u_{pr,\alpha}^{S'} = u_{pr,\alpha}^S - \langle u_{pr,\alpha}^S \rangle_p, \quad u_{f,\alpha}^{S'} = u_{f,\alpha}^S - \langle u_{f,\alpha}^S \rangle_p. \quad (9)$$

The relation (8) shows that the energy of the particle velocity fluctuations can be decomposed into one contribution stemming from the particles' relative motion with respect to the surrounding fluid (first term on the right-hand-side in 8), one contribution due to the fluctuations of the fluid velocity in the vicinity of the particles (second term on the r.h.s. of 8), and one contribution due to the correlation between the former two (last term in 8). Figure 24 shows the three contributions on the right-hand-side of (8) for the vertical direction ( $\alpha = 3$ ) along with the total fluctuation energy (note that this is the square of the quantity depicted in figure 6b). It can be seen that in both flow cases the contribution from the cross-correlation  $\langle u_{pr,\alpha}^{S'} u_{f,\alpha}^{S'} \rangle_p$  is much smaller than the remaining

two terms, indicating that the fluctuations of the particle velocity are not strongly coupled to the velocity of the surrounding fluid. The variance of the fluid velocity seen by the particles,  $\langle w_f^{S'} w_f^{S'} \rangle_p$ , on the other hand, is the largest contribution in both flow cases. Its time evolution exhibits a similar shape as the total particle velocity fluctuation energy. In case M178 the time average value  $\langle w_f^{S'} w_f^{S'} \rangle_{p,t} / w_{ref}^2$  is three times as large as the corresponding value in case M121, making it the dominant term. Since the energy of fluctuations of the particle velocity relative to the surrounding fluid,  $\langle w_{pr}^{S'} w_{pr}^{S'} \rangle_p / w_{ref}^2$ , is approximately constant in time and of similar value in both flow cases (its time-average is 30% larger in case M178), it follows that the larger overall fluctuation energy in case M178 is mostly due to an increase of the fluctuation energy of the fluid velocity seen by the particles. The fact that the (vertical component of the) fluctuating particle velocity is – when taken relative to the surrounding fluid – of similar intensity in both cases indicates that the present difference in Galileo number does not significantly affect this quantity. However, the occurrence of particle clustering in case M178 does lead to a significant increase in the particle velocity fluctuation amplitude (as compared to the non-clustering case M121) by way of a difference in the surrounding fluid velocity which the particles experience (expressed through the term  $\langle w_f^{S'} w_f^{S'} \rangle_p$ ). Therefore, the effect of the Galileo number on the variance of the vertical particle velocity is of indirect nature.

The instantaneous angle  $\alpha$  (with respect to the vertical axis) of a particle's trajectory relative to the average fluid velocity is given by the following relation:

$$\tan \alpha = \sqrt{u_{pr}^2 + v_{pr}^2} / |w_{pr}|. \quad (10)$$

The probability density functions of  $\alpha$  are shown in figure 25. In both flow cases they roughly resemble a Gamma distribution. However, closer inspection shows that the right tails for sufficiently large  $\alpha$  are purely exponential (i.e.  $\text{pdf}(\alpha) \sim \exp(-a\alpha)$  with positive  $a$ ). As can be seen from the semi-logarithmic graph in figure 25(b), this exponential behavior is clearly exhibited by the data from case M178 for  $\alpha \gtrsim 15$  degrees, whereas in case M121 the pure exponential only matches a small range of angles around  $\alpha \approx 30$  degrees. The figure also shows that in case M178 the angle defined in (10) has a peak at approximately the value which is observed for an isolated sphere settling at the same density ratio and Galileo number (i.e.  $\alpha = 5.2$  degrees), but in the present case M178 it also exhibits a rather large standard deviation (equal to 4.3 degrees). In case M121, the peak of the corresponding pdf is found at a significantly smaller value of the angle ( $\alpha = 3.2$  degrees) and it has a comparatively smaller standard deviation (3.7 degrees). The most probable trajectory in case M178 is, therefore, inclined with respect to the vertical axis by a similar angle as in the case of an isolated sphere. In case M121 the most probable trajectory is relatively close to a vertical path (as in the corresponding single-sphere case). These results show that at the current solid volume fraction (and despite the agglomerations found in case M178) the particle motion is on average not too far removed from the state of motion of a corresponding isolated sphere. However, the collective effect manifests itself clearly in the form of broad probability distributions, i.e. frequent deviations from the most probable state.

The intensity of the angular particle velocity fluctuations is reported in figure 26(a). It can be observed that in both cases rotational motion around a horizontal axis is much more intense than the vertical component (by a factor of 6.0 and 2.7 in cases M121 and M178, respectively). This strong anisotropy is consistent with the corresponding difference in fluid velocity fluctuation intensities (cf. figure 6a): gradients of the vertical fluid velocity drive the horizontal component of the angular particle motion and vice versa. The large-scale fluid velocity fluctuations due to clustering in case M178, however, appear to have a small influence upon the overall intensity of the angular particle motion, presumably due to the fact that the cluster scale is significantly larger than the particle diameter. This is evident from the near-absence in figure 26(a) of temporal fluctuations of the same scales as in figure 6. Likewise, the increase in the horizontal angular velocity from case M121 to case M178 measures only 5%. We have also analyzed the statistical correlation between angular particle velocity and of the fluctuations of the Voronoi cell volumes. The graph in figure 26(b) shows that smaller cell volumes (i.e. larger local concentration values) lead to a significant increase in the standard deviation of the angular velocity in the clustering



case M178, both for the horizontal and the vertical components in very similar fashion. In the non-clustering case M121, on the contrary, the standard deviation of all components of the angular particle velocity is approximately independent of the Voronoï cell volume. The exception is a non-monotonous decrease observed at very small cell volumes (below 50 times the particle volume). Please note that the number of samples decreases considerably at small values of the Voronoï cell volume in case M121 which leads to significant oscillations of the curve. It is noteworthy from the analysis of figure 26(b) that the Voronoï cell volume (i.e. the local particle concentration) does not by itself constitute a good indicator of an increase of the amplitude of angular particle motion. It does so only in conjunction with the knowledge of the occurrence of particle clustering, which can be deduced e.g. from the standard deviation of Voronoï cell volumes (cf. figure 12).

## 4 Summary and conclusions

We have simulated the gravity-induced motion of randomly distributed, finite-size, heavy particles in otherwise quiescent fluid in triply-periodic domains. Focusing on a solid-to-fluid density ratio of 1.5 and on a solid volume fraction of 0.005, we have considered two values of the Galileo number, measuring 121 and 178. Isolated spheres at the same density ratio and Galileo numbers settle steadily on a vertical and on an oblique path, respectively. In the multi-particle case, strong clustering of particles in the form of vertically-elongated columnar regions is observed at the higher Galileo number value. This result is consistent with the finding of Kajishima (2004) at  $Ga \approx 210$ . At the smaller Galileo number the particle arrangement found in the present study can actually be characterized as slightly more ordered than a distribution through a random Poisson process. The observed clusters in the present work have horizontal extensions equivalent to some 10 particle diameters; in the vertical direction they essentially extend throughout the entire domain length of 170 particle diameters.

In the clustering case, Voronoï tessellation analysis further reveals that approximately 30% of the particles reside in cluster regions at a given instant in time, and that their residence time both in clusters and in void regions is long compared to the gravitational time scale.

Through comparison between the two flow cases the current configuration allows us to investigate the impact of clustering upon the particle motion in detail. It is found that clustering leads to a significant increase of the magnitude of the average settling velocity measured relative to the volume-averaged fluid velocity (by 12% as compared to the value obtained for an isolated particle). Using our definition of the fluid velocity in the vicinity of the (finite-size) particles we deduce that the particles in the clustering case sample the fluid field preferentially in regions of downward motion (when compared to the box-averaged fluid velocity value). As a consequence, the relative velocity between the phases – when based upon the local fluid velocity “seen” by the particles – is similar to the one of a corresponding isolated particle at both investigated Galileo numbers. This finding suggests that it may be possible to approximate the particle settling velocity as the sum of two contributions, adding the characteristic meso-scale velocity of the surrounding fluid to the settling velocity value of an isolated sphere. This idea was suggested by an anonymous referee in analogy to the model proposed by Aliseda *et al.* (2002) for the enhancement of the settling velocity of sub-Kolmogorov-size droplets due to clustering in grid-generated turbulence. In their case it was possible to model the additional term as a function of the local particle concentration by identifying the particle clusters with macro-particles of a linear dimension equivalent to the experimentally determined cluster size; invoking Stokes flow and using a concentration-dependent mixture density the model was successful in reproducing the experimental trends. In the present case, however, the assumption of Stokes flow is not appropriate, and the dependency of the settling velocity upon the local concentration is not linear, as seen in figure 17. Furthermore, our study features only a single case with significant particle clustering. Therefore, additional data (at different solid volume fractions and Galileo numbers) is required in order to further pursue this avenue.

Concerning the fluctuations of the particle motion, it is found that simple superposition of isolated sphere data cannot account for the observed amplitudes of the multi-particle system. A

decomposition of the variance of the particle velocity is proposed which separates the contribution due to the particle motion with respect to the surrounding fluid from the contribution due to the fluctuations of the fluid velocity in the vicinity of the particles. In the clustering case the time-averaged variance of the vertical particle velocity is more than twice as large as in the non-clustering case. The decomposition shows that this increase is mainly due to a three-fold increase in the latter contribution (i.e. the variance of the fluid velocity surrounding the particles). Therefore, the observed increase in the particle velocity fluctuation amplitude in that case is due to a substantial amount of particles being located in clusters or void regions which constitute large scale fluid velocity perturbations with respect to the box-averaged value.

In the present work we have also analyzed the micro-structure of the particulate phase in detail. The particle-conditioned solid volume fraction has revealed that clustering not only manifests itself through a very slowly decaying excess of particles vertically above a test particle, but that it also leads to a significantly increased probability of finding particles at small horizontal distances of several diameters from the test particle. For the clustering case, particle-conditioned averaging also shows that the settling velocity of particles located inside a roughly cylindrical region with diameter equivalent to approximately  $10D$  surrounding a test particle are settling at a higher speed than the global average. Since a large number of particles resides in regions of increased particle concentration in this case, the pattern of increased settling speed is consistent with the geometry of the clusters themselves.

A further analysis of the fluid flow induced by the settling particles (such as a characterization of the pseudo-turbulence, particle-conditioned averaging of the near field, etc.) has not been performed in the current paper. This will be the subject of a future publication.

One question of interest obviously concerns the mechanism of particle cluster formation. Wake attraction in the sense of “drafting-kissing-tumbling” (cf. Fortes *et al.*, 1987; Wu & Manasseh, 1998) has already been identified as the key ingredient in the process (Kajishima, 2004). However, the details of cluster formation still await further clarification before modelling of the phenomenon becomes possible. In particular, with respect to the present results it is not clear how (for otherwise identical parameters) a critical value of the Galileo number for the appearance of clustering arises. In the present work we have not attempted to obtain a more precise value of the critical Galileo number due to the high computational cost associated to the additional simulations which would be required. However, it is now established that for a value of  $Ga = 121$  (whence an isolated sphere settles on a straight path) no clustering takes place, while at  $Ga = 178$  (corresponding to an oblique path for an isolated sphere) clustering is observed. The lateral motion of isolated particles (with random orientation) may promote the tendency to cluster in dilute multi-particle systems by increasing the probability of close particle encounters, which then – through said “drafting” effect – lead to statistically significant accumulations. From this observation it appears tempting to relate the onset of clustering to the bifurcation point (from axi-symmetric to planar-oblique) of the wake of an isolated sphere – at least under similarly dilute conditions as in the present case. This conjecture would mark the critical point at a Galileo value of approximately 155.

As a future perspective, we believe it will be worthwhile to determine the critical Galileo number for the onset of clustering more precisely. Near that threshold it should then be possible to determine whether the decisive factor triggering cluster formation is indeed related to the tendency of particles to follow non-vertical paths or possibly due to an alternative mechanism.

Thanks is due to J. Dušek for fruitful discussions. This work was supported by the German Research Foundation (DFG) under projects UH 242/1-1 and UH 242/1-2. The simulations were partially performed at Jülich Supercomputing Center (grant hka09), at LRZ München (grant pr58cu) and at SCC Karlsruhe. The computer resources, technical expertise and assistance provided by these centers are gratefully acknowledged.

## A Averaging procedures

The current appendix provides detailed definitions of the various averaging operators used in the present work.

## A.1 Phase averaging

Let us first define indicator functions for both the fluid and the dispersed phase. An indicator function for the fluid phase  $\Phi_f(\mathbf{x}, t)$  specifies whether a given point  $\mathbf{x}$  at time  $t$  is located inside the region  $\Omega_f(t)$  occupied by the fluid at time  $t$ , viz.

$$\Phi_f(\mathbf{x}, t) = \begin{cases} 1 & \text{if } \mathbf{x} \in \Omega_f(t) \\ 0 & \text{else} \end{cases}. \quad (11)$$

The corresponding indicator function for the dispersed phase  $\Phi_p(\mathbf{x}, t)$  can be readily obtained as:

$$\Phi_p(\mathbf{x}, t) = 1 - \Phi_f(\mathbf{x}, t). \quad (12)$$

Based on the definitions in equations (11) and (12) a discrete counter of sample points occupied by the carrier phase,  $n_f$ , and by the dispersed phase,  $n_p$ , at time  $t^m$  can be defined as follows (with subscript  $\alpha = f$  or  $\alpha = p$ ):

$$n_\alpha(t^m) = \sum_{i=1}^{N_x} \sum_{j=1}^{N_y} \sum_{k=1}^{N_z} \Phi_\alpha(\mathbf{x}_{ijk}, t^m) \quad \forall m \in [1, N_t^{(\alpha)}], \quad (13)$$

where  $N_x$ ,  $N_y$  and  $N_z$  are the number of grid nodes in the corresponding coordinate directions,  $\mathbf{x}_{ijk}$  is the spatial location of a grid node with indices  $i$ ,  $j$ ,  $k$ , and  $N_t^{(f)}$  ( $N_t^{(p)}$ ) is the number of available instantaneous flow fields (particle states).

The fluid-phase averaging for any fluid-related quantity  $\psi_f(\mathbf{x}_{ijk}, t^m)$  at time  $t^m$  can be defined as:

$$\langle \psi_f \rangle_{\Omega_f}(t^m) = \frac{1}{n_f(t^m)} \sum_{i=1}^{N_x} \sum_{j=1}^{N_y} \sum_{k=1}^{N_z} \Phi_f(\mathbf{x}_{ijk}, t^m) \psi_f(\mathbf{x}_{ijk}, t^m), \quad \forall m \in [1, N_t^{(f)}]. \quad (14)$$

Similarly, by defining a counter of fluid phase samples along the vertical direction,  $n_f^{(z)}$ , viz.

$$n_f^{(z)}(x_i, y_j, t^m) = \sum_{k=1}^{N_z} \Phi_f(\mathbf{x}_{ijk}, t^m) \quad \forall m \in [1, N_t^{(f)}], i \in [1, N_x], j \in [1, N_y], \quad (15)$$

the spatial average of a fluid-related quantity  $\psi_f(\mathbf{x}_{ijk}, t^m)$  over the vertical direction is defined as follows:

$$\langle \psi_f \rangle_z(x_i, y_j, t^m) = \frac{1}{n_f^{(z)}(x_i, y_j, t^m)} \sum_{k=1}^{N_z} \Phi_f(\mathbf{x}_{ijk}, t^m) \psi_f(\mathbf{x}_{ijk}, t^m), \quad (16)$$

$$\forall m \in [1, N_t^{(f)}], i \in [1, N_x], j \in [1, N_y].$$

The dispersed-phase averaging operator  $\langle \cdot \rangle_p$  for a given quantity  $\psi_p^i(t^m)$  related to the  $i$ th particle at time  $t^m$  can be defined as:

$$\langle \psi_p \rangle_p(t^m) = \frac{1}{N_p} \sum_{i=1}^{N_p} \psi_p^i(t^m), \quad \forall m \in [1, N_t^{(p)}]. \quad (17)$$

A time-averaging operator for any quantity  $\psi(t^m)$  related to either the dispersed phase or the carrier phase can be defined as follows:

$$\langle \psi \rangle_t = \frac{1}{N_t^{(\alpha)}} \sum_{m=1}^{N_t^{(\alpha)}} \psi(t^m), \quad (18)$$

where  $\alpha = p$  or  $\alpha = f$ , respectively.

Combining the operators defined in (14) and (18), the time and space average of a fluid quantity  $\langle \psi_f \rangle_{\Omega_f, t}$  is obtained. Analogously, the average of a particle-related quantity over all available particle samples,  $\langle \psi_p \rangle_{p, t}$ , is defined from the combination of operators (17) and (18).

## A.2 Particle-conditioned averaging

Let us first define a three-dimensional averaging domain  $\Omega_A$  with grid node locations  $\mathbf{y}_{ijk}$ . The averaging domain  $\Omega_A$  is discretized in the same manner as the simulations, i.e. with an isotropic mesh with constant grid spacing in all spatial directions. The averaging domain is first shifted to the position of one of the particles. Then the instantaneous coordinate of a grid node  $\mathbf{y}_{ijk} \in \Omega_A$  relative to the position of the  $l$ -th particle is defined as:

$$\tilde{\mathbf{x}}_{ijk}^l(t^m) = \mathbf{y}_{ijk} - \mathbf{x}_p^l(t^m), \quad \forall m \in [1, N_{p,t}], \quad l = 1 \dots N_p. \quad (19)$$

We can now define a discrete counter field  $\tilde{n}_{ijk}^p(\mathbf{y}_{ijk})$  which holds the number of samples obtained through dispersed-phase averaging at a given grid node in the averaging domain  $\Omega_A$  at time  $t^m$ :

$$\tilde{n}_{ijk}^p(\tilde{\mathbf{x}}_{ijk}) = \sum_{m=1}^{N_{p,t}} \sum_{l=1}^{N_p} \Phi_p(\tilde{\mathbf{x}}_{ijk}^l(t^m), t^m), \quad (20)$$

where  $\Phi_p$  is defined in (12). Under proper normalization, the quantity  $\tilde{n}_{ijk}^p(\tilde{\mathbf{x}}_{ijk})$  defines the particle-conditioned local solid volume fraction  $\phi_s^{cond}$ , viz.

$$\phi_s^{cond}(\tilde{\mathbf{x}}_{ijk}) = \frac{1}{N_{p,t} N_p} \tilde{n}_{ijk}^p(\tilde{\mathbf{x}}_{ijk}). \quad (21)$$

The particle-conditioned space-time averaging of any particle-related quantity  $\psi_p^l(t^m)$  can then be defined as follows:

$$\psi_p^{cond}(\tilde{\mathbf{x}}_{ijk}) = \frac{1}{\tilde{n}_{ijk}^p(\tilde{\mathbf{x}}_{ijk})} \sum_{m=1}^{N_{p,t}} \sum_{l=1}^{N_p} \Phi_p(\tilde{\mathbf{x}}_{ijk}^l(t^m), t^m) \psi_p^l(t^m). \quad (22)$$

## References

- ALISEDA, A., CARTELLIER, A., HAINAUX, F. & LASHERAS, J.C. 2002 Effect of preferential concentration on the settling velocity of heavy particles in homogeneous isotropic turbulence. *J. Fluid Mech.* **468**, 77–105.
- BAGCHI, P. & BALACHANDAR, S. 2003 Effect of turbulence on the drag and lift of a particle. *Phys. Fluids* **15** (11), 3496–3513.
- BEETSTRA, R., VAN DER HOEF, M.A. & KUIPERS, J.A.M. 2007 Drag force of intermediate Reynolds number flow past mono- and bidisperse arrays of spheres. *AIChE J.* **53** (2), 489–501.
- BOUCHET, G., MEBAREK, M. & DUŠEK, J. 2006 Hydrodynamic forces acting on a rigid fixed sphere in early transitional regimes. *Eur. J. Mech. B/Fluids* **25**, 321–336.
- CARTELLIER, ALAIN, ANDREOTTI, MARCELO & SECHET, PHILIPPE 2009 Induced agitation in homogeneous bubbly flows at moderate particle reynolds number. *Phys. Rev. E* **80**, 065301.
- CHAN-BRAUN, C., GARCÍA-VILLALBA, M. & UHLMANN, M. 2011 Force and torque acting on particles in a transitionally rough open channel flow. *J. Fluid Mech.* **684**, 441–474.
- CHAN-BRAUN, C., GARCÍA-VILLALBA, M. & UHLMANN, M. 2013 Spatial and temporal scales of force and torque acting on wall-mounted spherical particles in open channel flow. *Phys. Fluids* **25** (7), 075103.
- CISSE, M., HOMANN, H. & BEC, J. 2013 Slipping motion of large neutrally buoyant particles in turbulence. *J. Fluid Mech.* **735**.

- FERENC, J.-S. & NEDA, Z. 2007 On the size distribution of Poisson Voronoi cells. *Physica A* **385**.
- FESSLER, J.R., KULICK, J.D. & EATON, J.K. 1994 Preferential concentration of heavy particles in a turbulent channel flow. *Phys. Fluids* **6** (11), 3742–3749.
- FORTES, A.F., JOSEPH, D.D. & LUNDGREN, T.S. 1987 Nonlinear mechanics of fluidization of beds of spherical particles. *J. Fluid Mech.* **177**, 467–483.
- GARCÍA-VILLALBA, M., KIDANEMARIAM, A.G. & UHLMANN, M. 2012 DNS of vertical plane channel flow with finite-size particles: Voronoi analysis, acceleration statistics and particle-conditioned averaging. *Int. J. Multiphase Flow* **46**, 54–74.
- GHIDERSA, B. & DUŠEK, J. 2000 Breaking of axisymmetry and onset of unsteadiness in the wake of a sphere. *J. Fluid Mech.* **423**, 33–69.
- GLOWINSKI, R., PAN, T.-W., HESLA, T.I. & JOSEPH, D.D. 1999 A distributed Lagrange multiplier/fictitious domain method for particulate flows. *Int. J. Multiphase Flow* **25**, 755–794.
- HILL, R.J., KOCH, D.L. & LADD, A.J.C. 2001 Moderate-Reynolds-number flows in ordered and random arrays of spheres. *J. Fluid Mech.* **448**, 243–278.
- HOROWITZ, M. & WILLIAMSON, C.H.K. 2010 The effect of Reynolds number on the dynamics and wakes of freely rising and falling spheres. *J. Fluid Mech.* **651** (251-294).
- JENNY, M., DUŠEK, J. & BOUCHET, G. 2004 Instabilities and transition of a sphere falling or ascending freely in a Newtonian fluid. *J. Fluid Mech.* **508**, 201–239.
- JEONG, J. & HUSSAIN, F. 1995 On the identification of a vortex. *J. Fluid Mech.* **285**, 69–94.
- JOHNSON, T.A. & PATEL, V.C. 1999 Flow past a sphere up to a Reynolds number of 300. *J. Fluid Mech.* **378**, 19–70.
- KAJISHIMA, T. 2004 Influence of particle rotation on the interaction between particle clusters and particle-induced turbulence. *Int. J. Heat Fluid Flow* **25** (5), 721–728.
- KAJISHIMA, T. & TAKIGUCHI, S. 2002 Interaction between particle clusters and particle-induced turbulence. *Int. J. Heat Fluid Flow* **23**, 639–646.
- KIDANEMARIAM, A.G., CHAN-BRAUN, C., DOYCHEV, T. & UHLMANN, M. 2013 DNS of horizontal open channel flow with finite-size, heavy particles at low solid volume fraction. *New J. Phys.* **15** (2), 025031.
- KIM, I., ELGHOBASHI, S. & SIRIGNANO, W.A. 1993 Three-dimensional flow over two spheres placed side by side. *J. Fluid Mech.* **246**, 465–488.
- LANCE, M. & BATAILLE, J. 1991 Turbulence in the liquid phase of a uniform bubbly air-water flow. *J. Fluid Mech.* **222**, 95–118.
- LUCCI, F., FERRANTE, A. & ELGHOBASHI, S. 2010 Modulation of isotropic turbulence by particles of Taylor length-scale size. *J. Fluid Mech.* **650**, 5–55.
- MARTINEZ-MERCADO, J., PALACIOS-MORALES, C.A. & ZENIT, R. 2007 Measurement of pseudoturbulence intensity in monodispersed bubbly liquids for  $10 \leq \text{Re} \leq 500$ . *Phys. Fluids* **19** (10), 103302.
- MELHEIM, J.A. 2005 Cluster integration method in Lagrangian particle dynamics. *Comput. Phys. Commun.* **171** (3), 155–161.
- MERLE, A., LEGENDRE, D. & MAGNAUDET, J. 2005 Forces on a high-Reynolds-number spherical bubble in a turbulent flow. *J. Fluid Mech.* **532**, 53–62.

- MIZUKAMI, M., PARTHASARATHY, R.N. & FAETH, G.M. 1992 Particle-generated turbulence in homogeneous dilute dispersed flows. *Int. J. Multiphase Flow* **18** (3), 397 – 412.
- MONCHAUX, R., BOURGOIN, M. & CARTELLIER, A. 2010a Inertial particles clustering in turbulent flows: a Voronoi analysis. In *ICMF 2010* (ed. S. Balachandar & J. Sinclair Curtis). Tampa, USA: CDROM.
- MONCHAUX, R., BOURGOIN, M. & CARTELLIER, A. 2010b Preferential concentration of heavy particles: A Voronoi analysis. *Phys. Fluids* **22**, 103304.
- MONCHAUX, R., BOURGOIN, M. & CARTELLIER, A. 2012 Analyzing preferential concentration and clustering of inertial particles in turbulence. *Int. J. Multiphase Flow* **40**, 1–18.
- OKABE, A., BOOTS, B., SUGIHARA, K. & CHIU, S.N. 1992 *Spatial tessellations: concepts and applications of Voronoi diagrams*. Wiley.
- PARTHASARATHY, R.N. & FAETH, G.M. 1990a Turbulence modulation in homogeneous dilute particle-laden flows. *J. Fluid Mech.* **220**, 485–514.
- PARTHASARATHY, R.N. & FAETH, G.M. 1990b Turbulent dispersion of particles in self-generated homogeneous turbulence. *J. Fluid Mech.* **220**, 515–537.
- RIBOUX, G., LEGENDRE, D. & RISSO, F. 2013 A model of bubble-induced turbulence based on large-scale wake interactions. *J. Fluid Mech.* **719**, 362–387.
- RIBOUX, G., RISSO, F. & LEGENDRE, D. 2010 Experimental characterization of the agitation generated by bubbles rising at high Reynolds number. *J. Fluid Mech.* **643**, 509.
- RISSO, F. 2011 Theoretical model for  $k^{-3}$  spectra in dispersed multiphase flows. *Phys. Fluids* **23** (1), 011701.
- RISSO, F. & ELLINGSEN, K. 2002 Velocity fluctuations in a homogeneous dilute dispersion of high-Reynolds-number rising bubbles. *J. Fluid Mech.* **453**, 395–410.
- RISSO, F., ROIG, V., AMOURA, Z., RIBOUX, G. & BILLET, A.-M. 2008 Wake attenuation in large Reynolds number dispersed two-phase flows. *Phil. Trans. Royal Soc. A* **366** (1873), 2177–2190.
- SARDINA, G., SCHLATTER, P., BRANDT, L., PICANO, F. & CASCIOLA, C. M. 2012 Wall accumulation and spatial localization in particle-laden wall flows. *J. Fluid Mech.* **699**, 50–78.
- SCHOUVEILER, L., BRYDON, A., LEWEKE, T. & THOMPSON, M.C. 2004 Interactions of the wakes of two spheres placed side by side. *European J. Mechanics - B/Fluids* **23** (1), 137 – 145.
- SCHOUVEILER, L. & PROVENSALE, M. 2002 Self-sustained oscillations in the wake of a sphere. *Phys. Fluids* **14** (11), 3846–3854.
- SHOTORBAN, B. & BALACHANDAR, S. 2006 Particle concentration in homogeneous shear turbulence simulated via Lagrangian and equilibrium Eulerian approaches. *Phys. Fluids* **18**, 065105.
- SUNDARAM, S. & COLLINS, L.R. 1997 Collision statistics in an isotropic particle-laden turbulent suspension. Part 1. Direct numerical simulations. *J. Fluid Mech.* **335**, 75–109.
- TENNETTI, S., GARG, R. & SUBRAMANIAM, S. 2011 Drag law for monodisperse gas-solid systems using particle-resolved direct numerical simulation of flow past fixed assemblies of spheres. *Int. J. Multiphase Flow* **37**, 1072–1092.
- TSUJI, T., NARUTOMI, R., YOKOMINE, T., EBARA, S. & SHIMIZU, A. 2003 Unsteady three-dimensional simulation of interactions between flow and two particles. *Int. J. Multiphase Flow* **29** (9), 1431 – 1450.

- TSUJI, Y., MORIKAWA, Y. & TERASHIMA, K. 1982 Fluid-dynamic interaction between two spheres. *Int. J. Multiphase Flow* **8** (1), 71–82.
- UHLMANN, M. 2004 New results on the simulation of particulate flows. Technical Report No. 1038, CIEMAT, Madrid, Spain, ISSN 1135-9420.
- UHLMANN, M. 2005*a* An immersed boundary method with direct forcing for the simulation of particulate flows. *J. Comput. Phys.* **209** (2), 448–476.
- UHLMANN, M. 2005*b* An improved fluid-solid coupling method for DNS of particulate flow on a fixed mesh. In *Proc. 11th Workshop Two-Phase Flow Predictions* (ed. M. Sommerfeld). Merseburg, Germany: Universität Halle, ISBN 3-86010-767-4.
- UHLMANN, M. 2006 Experience with DNS of particulate flow using a variant of the immersed boundary method. In *Proc. ECCOMAS CFD 2006* (ed. P. Wesseling, E. Oñate & J. Périaux). Egmond aan Zee, The Netherlands: TU Delft, iISBN 90-9020970-0.
- UHLMANN, M. 2008 Interface-resolved direct numerical simulation of vertical particulate channel flow in the turbulent regime. *Phys. Fluids* **20** (5), 053305.
- UHLMANN, M. & DUŠEK, J. 2014 The motion of a single heavy sphere in ambient fluid: a benchmark for interface-resolved particulate flow simulations with significant relative velocities. *Int. J. Multiphase Flow* **59**, 221–243.
- VELDHUIS, C.H.J. & BIESHEUVEL, A. 2007 An experimental study of the regimes of motion of spheres falling or ascending freely in a newtonian fluid. *Int. J. Multiphase Flow* **33** (10), 1074–1087.
- WU, J. & MANASSEH, R. 1998 Dynamics of dual-particles settling under gravity. *Int. J. Multiphase Flow* **24**, 1343–1358.
- WYLIE, J.J. & KOCH, D.L. 2000 Particle clustering due to hydrodynamical interactions. *Phys. Fluids* **12** (5), 964–970.
- YIN, X. & KOCH, D.L. 2008 Velocity fluctuations and hydrodynamic diffusion in finite-Reynolds-number sedimenting suspensions. *Phys. Fluids* **20** (4), 043305.

case	$\Phi_s$	$\rho_p/\rho_f$	$Ga$	$Re$	$L_x \times L_y \times L_z$	$N_p$	$T_{obs}/\tau_g$
M121	$5 \cdot 10^{-3}$	1.5	121.24	141.6	$68D \times 68D \times 341D$	15190	2967
M178	$5 \cdot 10^{-3}$	1.5	178.46	260.6	$85D \times 85D \times 170D$	11867	1472
S121	$5.3 \cdot 10^{-5}$	1.5	121.24	141.1	$8.5D \times 8.5D \times 136D$	1	–
S178	$2.7 \cdot 10^{-5}$	1.5	178.46	233.1	$10.6D \times 10.6D \times 170D$	1	–

Table 1: Physical parameters in the present simulations: global solid volume fraction  $\Phi_s$ , density ratio  $\rho_p/\rho_f$ , Galileo number  $Ga = u_g D/\nu$ , Reynolds number  $Re = |\langle w_s \rangle_t| D/\nu$  (based on the average settling velocity  $\langle w_s \rangle_t$  defined in equation 2, particle diameter  $D$  and fluid viscosity  $\nu$ ), size of the computational domain  $L_\alpha$  (in the coordinate direction  $x_\alpha$ ) and the number of particles  $N_p$ .  $T_{obs}$  is the duration of the observation interval over which statistics were accumulated.

case	$D/\Delta x$	$N_x \times N_y \times N_z$
M121	15	$1024 \times 1024 \times 5120$
M178	24	$2048 \times 2048 \times 4096$
S121	15	$128 \times 128 \times 2048$
S178	24	$256 \times 256 \times 4096$

Table 2: Numerical parameters employed in the present simulations. Particle resolution  $D/\Delta x$ , number of grid nodes  $N_i$  in the  $i$ -th coordinate direction.

case	$(\langle w_f^S \rangle_{p,t} - \langle w_f \rangle_{\Omega_f,t})/w_{ref}$	$\sigma_{p,t}(w_f^S)/w_{ref}$	$\sigma_{\Omega_f,t}(w_f)/w_{ref}$
M121	−0.0315	0.1262	0.2081
M178	−0.1155	0.1972	0.2407

Table 3: The difference (in the mean and in the standard deviation) between the particle-conditioned vertical fluid velocity  $w_f^S(i,t)$  ( $\forall i = 1 \dots N_p$ ) and the unconditioned velocity field  $w_f(\mathbf{x} \in \Omega_f, t)$ . The operator  $\sigma_{p,t}$  refers to the standard deviation with respect to the ensemble of particles and temporal snapshots;  $\sigma_{\Omega_f,t}$  denotes the standard deviation with respect to all available samples in the fluid phase and the available temporal records. All values are normalized with the absolute value of the conventional time-average settling velocity, i.e.  $w_{ref} = |\langle w_s(t) \rangle_t|$  (cf. equation 2).



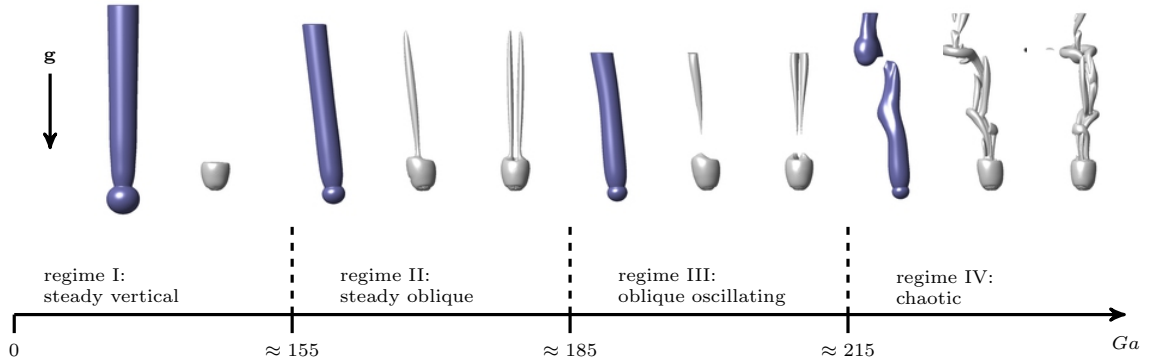


Figure 1: The four different regimes of particle motion encountered as a function of the Galileo number for a density ratio  $\rho_p/\rho_f = 1.5$ . In the upper part of the figure, the typical wake structure at one value of the Galileo number is shown for each regime (i.e. from left to right  $Ga = \{144, 178, 190, 250\}$ ). In each case, the blue surfaces indicate the locations where the fluid velocity relative to the particle in the direction given by its instantaneous velocity (i.e. the axial component) measures  $1.2u_g$ . The grey-colored surfaces are visualizations of the vortical structures by means of the  $\lambda_2$  criterion of Jeong & Hussain (1995). In regimes II-IV the vortical structures are additionally shown from a second viewpoint, rotated around the particle by an angle of  $\pi/2$  in the horizontal plane with respect to the first one. The regime boundaries ( $Ga = 155, 185, 215$ ) correspond to particle Reynolds numbers of approximately 203, 253 and 304, respectively. The flow data is from the study of Uhlmann & Dušek (2014).

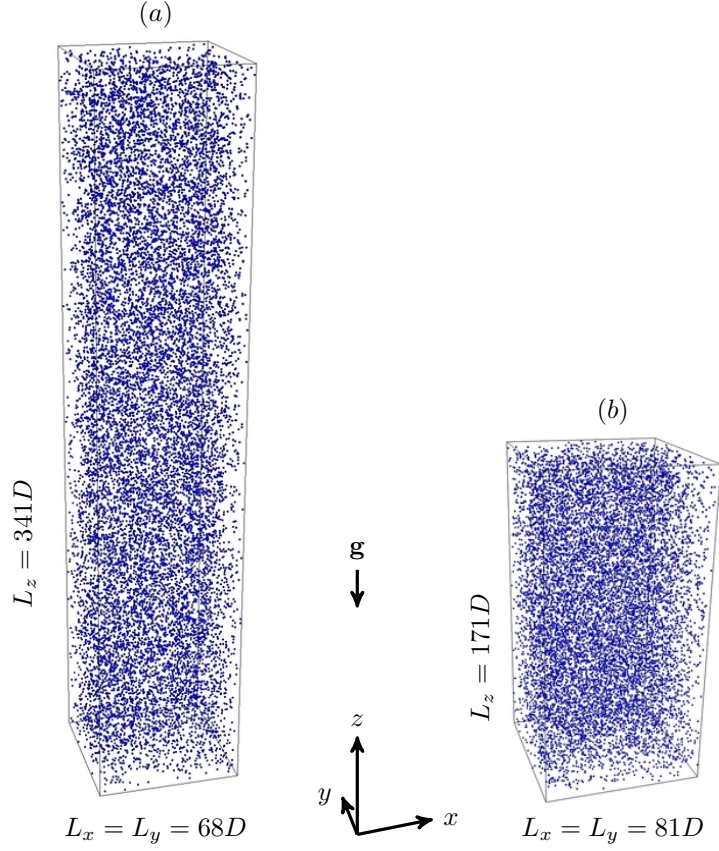


Figure 2: Dimensions of the computational domain with the initial particle distribution for (a) case M121 and (b) case M178.  $D$  denotes the particle diameter;  $\mathbf{g}$  is the vector of gravitational acceleration. Periodic boundary conditions are applied in all three spatial directions.

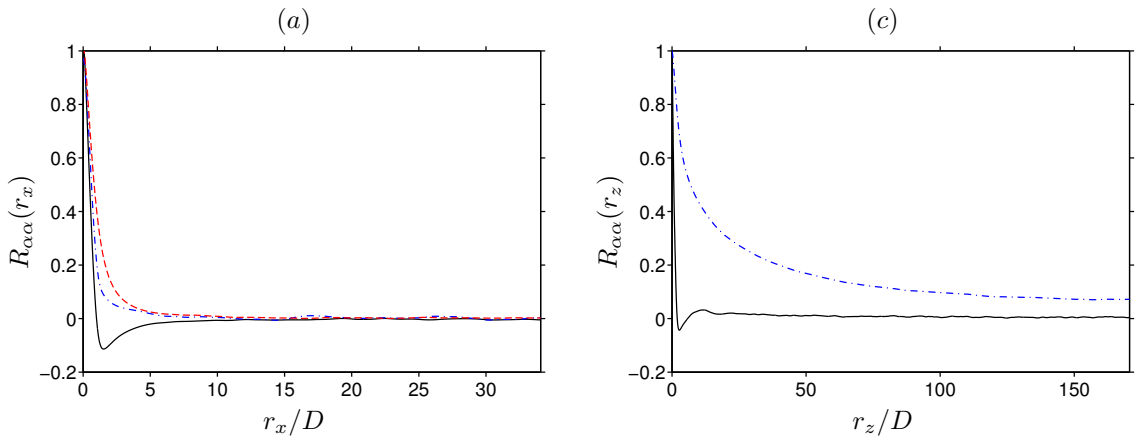


Figure 3: Two-point auto-correlation function of fluid velocity fluctuations in case M121 prior to release (i.e. at  $t = 0$ ), for separations in: (a) the  $x$ -direction, and (b) the  $z$ -direction. Lines show velocity components in the horizontal directions ( $u$ : —,  $v$ : - - -), and in the vertical direction ( $w$ : - · -). Note that in the graph in (b) the statistically equivalent component  $R_{22}(r_z)$  has been omitted.

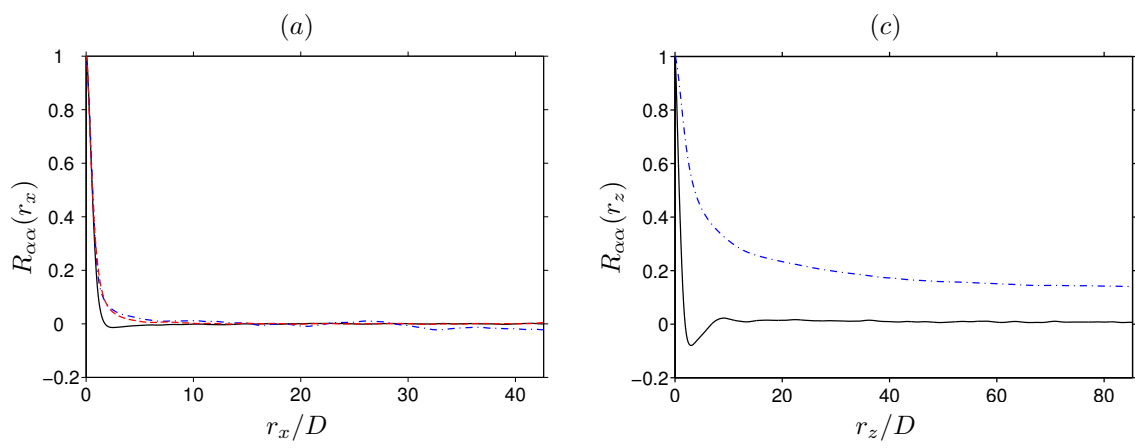


Figure 4: As in figure 3, but for case M178.

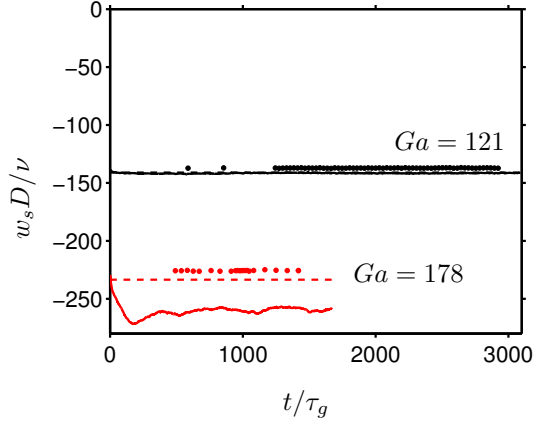


Figure 5: Average particle settling velocity as a function of time for both cases M121 and M178 (solid lines), normalized with the particle diameter and kinematic viscosity. The terminal velocity of a corresponding single particle (cases S121, S178) is indicated by dashed lines. The settling velocity with respect to the fluid velocity in the particles' vicinity (cf. discussion in § 3.3.1 and definition in equation 6) is indicated by filled circular symbols.

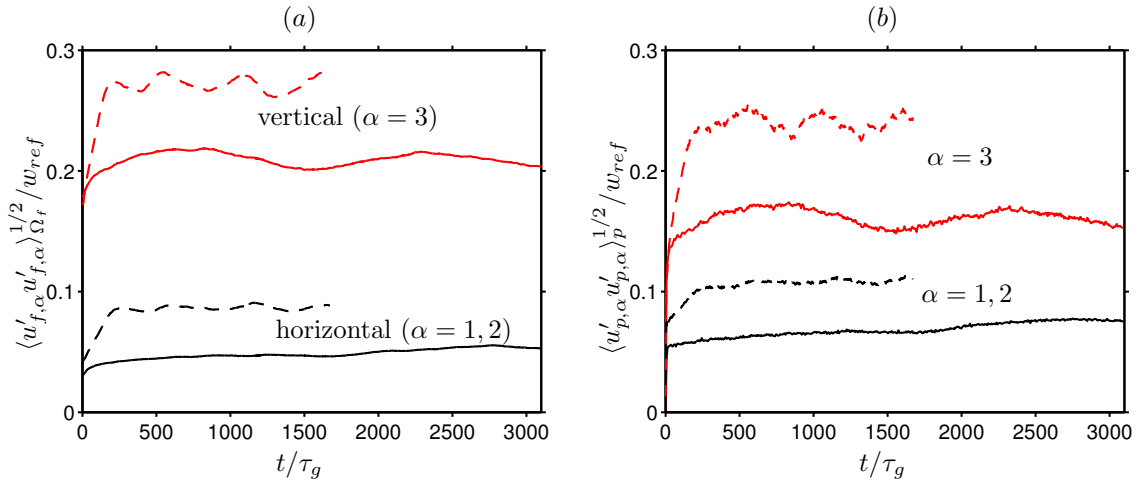


Figure 6: Intensity of the velocity fluctuations of: (a) the fluid phase, and (b) the particle phase. Results for case M121 (solid lines) and case M178 (dashed lines) are shown. As reference velocity  $w_{ref}$  for the purpose of normalization, the absolute value of the particle settling velocity  $|w_s|$  of the corresponding single-particle cases (S121 and S178, respectively) has been used.

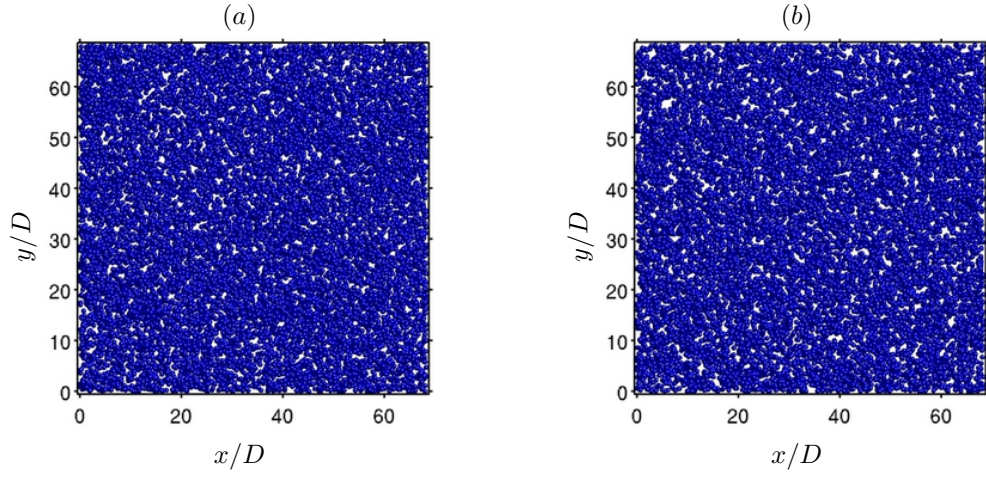


Figure 7: Particle positions in case M121 viewed from the top: (a) initial state at  $t = 0$ ; (b) in the statistically stationary regime at  $t = 1200\tau_g$ .

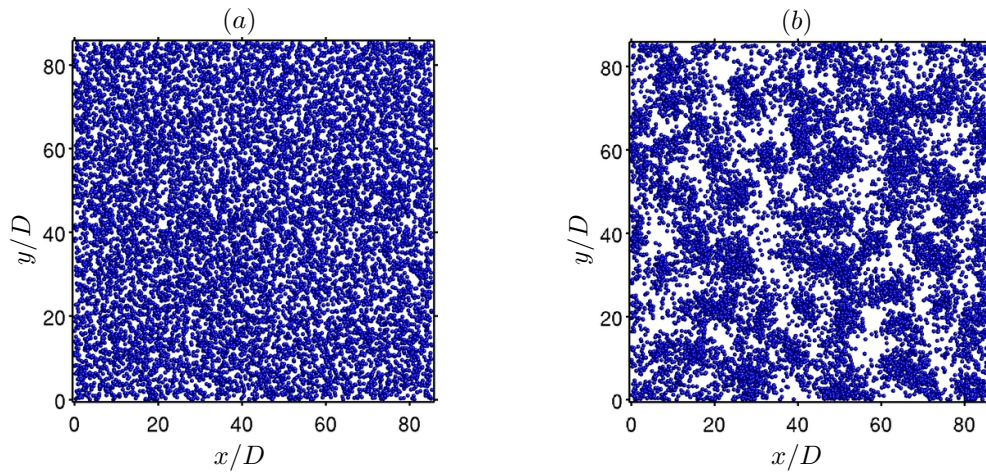


Figure 8: The same as figure 7, but for case M178: (a)  $t = 0$ ; (b)  $t = 820\tau_g$ .

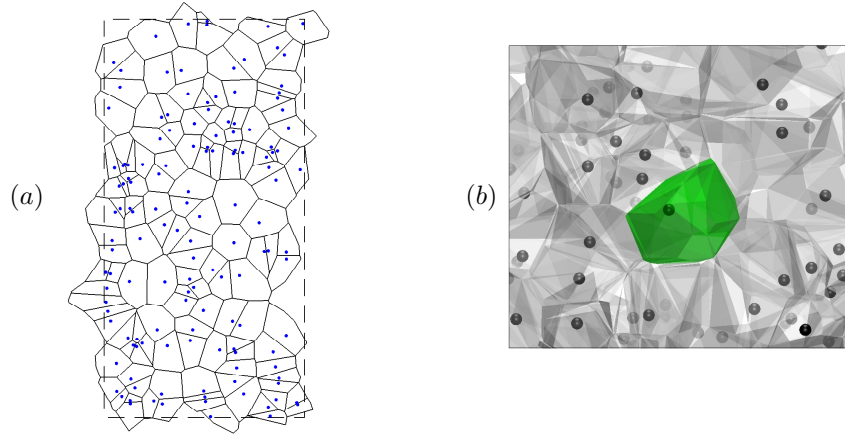


Figure 9: (a) A two dimensional Voronoi diagram in a vertical plane with double-periodic boundaries (indicated with dashed lines). The projected center locations of all particles intersecting the plane are taken as the Voronoi cell sites. Note that this graph is purely intended to illustrate the treatment of periodic directions; the actual analysis performed in this work considers the three-dimensional case. (b) Close-up of a three dimensional Voronoi diagram. Data is from case M178.

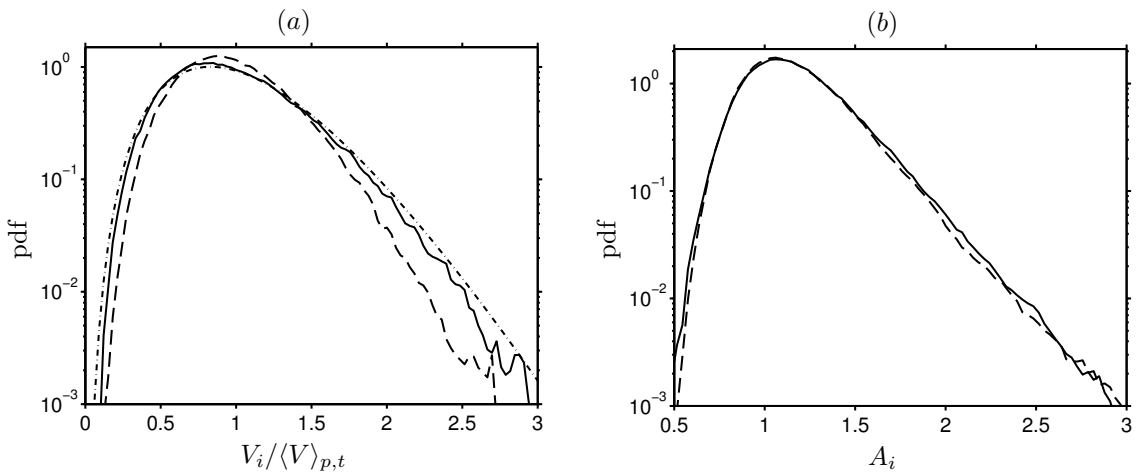


Figure 10: Case M121: probability density function of (a) the normalized Voronoi cell volumes  $V_i$  and (b) the Voronoi cell aspect ratios  $A_i$  defined in equation 3. Line styles correspond to different instants in time: the initial (random) particle distribution (solid line); the statistically stationary state (dashed line). In (a) the chain-dotted line represents the Gamma distribution corresponding to a random Poisson process (Ferenc & Neda, 2007).

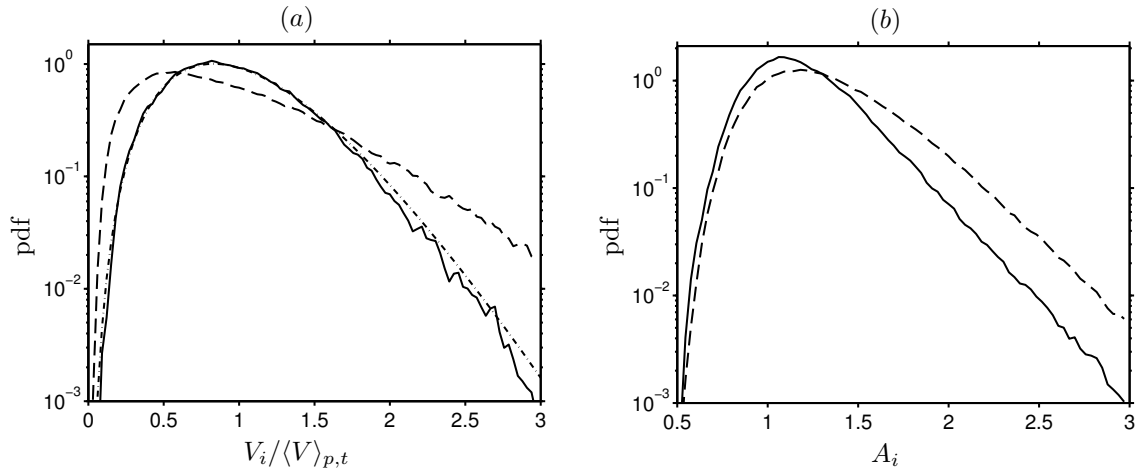


Figure 11: As figure 10, but for case M178.

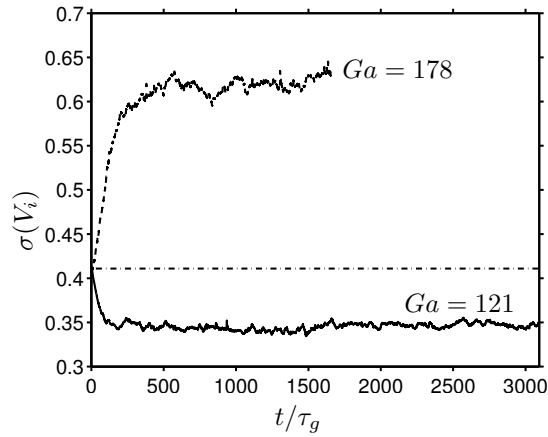


Figure 12: Standard deviation of Voronoi cell volumes as function of time: case M121 (solid line), case M178 (dashed line), randomly distributed particles (chain-dotted line).

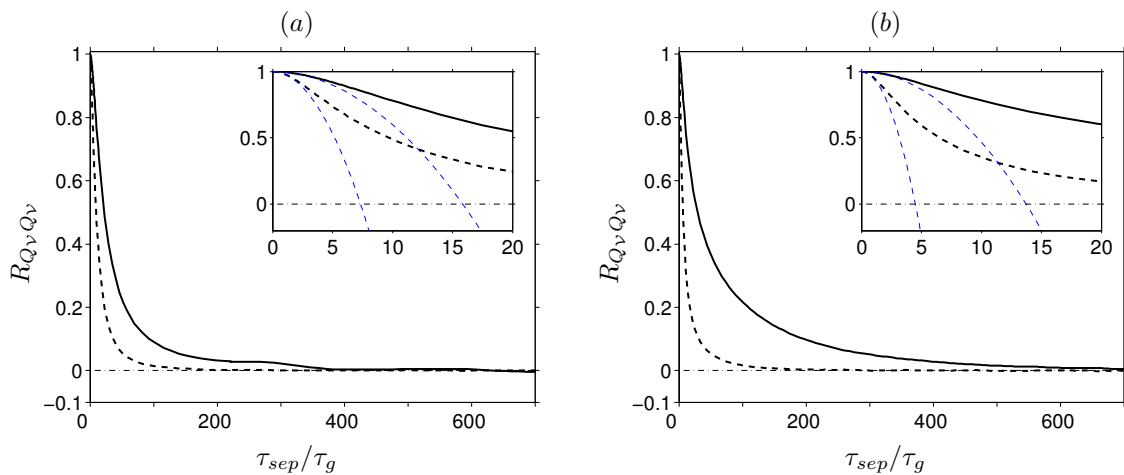


Figure 13: Lagrangian autocorrelation of Voronoi volumes  $R_{V_i V_i}$  (solid line) and of the Voronoi cell aspect ratio  $R_{A_i A_i}$  (dashed line) as function of the separation time  $\tau_{sep}$  (cf. definition in 4) for (a) case M121 and (b) case M178. The insets show closeups of the same data for small separations, including the osculating parabolas at  $\tau_{sep} = 0$ .

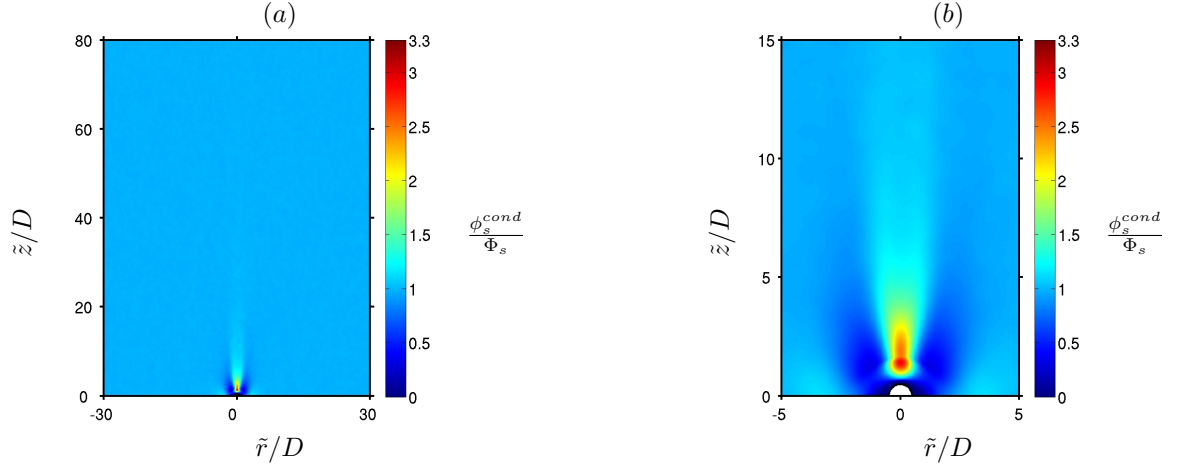


Figure 14: (a) Averaged solid volume fraction conditioned on particle positions for case M121, normalized by the global solid volume fraction. (b) Close-up of the same data. The coordinates  $\tilde{r}$  and  $\tilde{z}$  are relative to the test particle. Since the data is axi-symmetric,  $\tilde{r}$  denotes the distance in the horizontal plane.

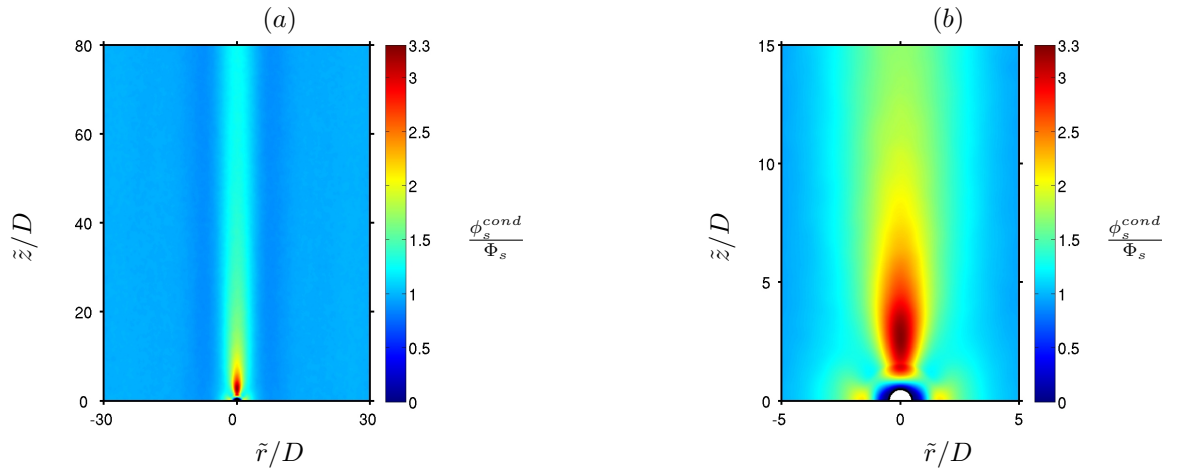


Figure 15: As figure 14, but for case M178.



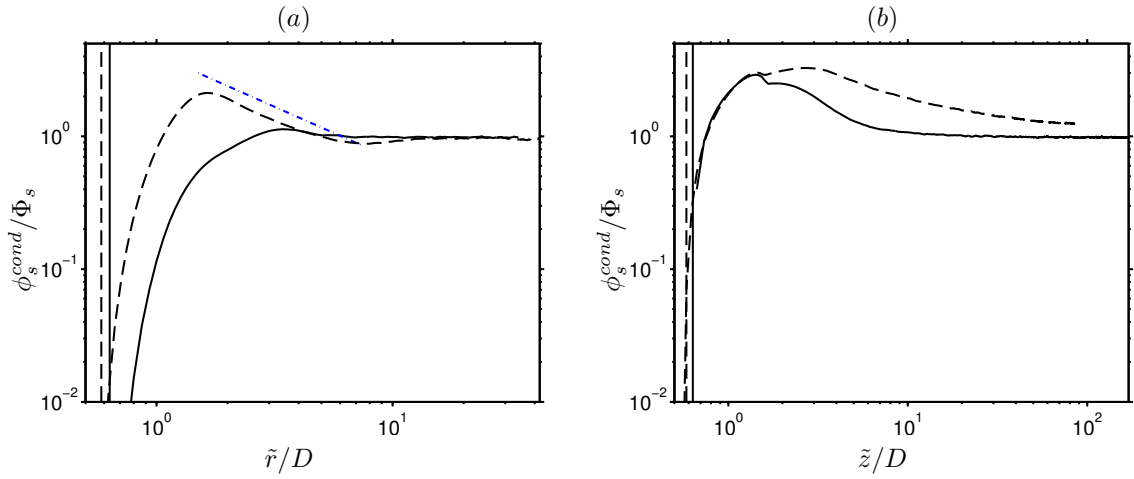


Figure 16: Variation of the particle-conditioned solid volume fraction  $\phi_s^{cond}$  along two perpendicular axes through the test particle: (a) for  $\tilde{z} = 0$ ; (b)  $\tilde{r} = 0$ . Shown are case M121 (solid line) and case M178 (dashed line). The vertical lines represent for each case the distance  $|\tilde{\mathbf{x}}_{ijk}| = D/2 + 2\Delta x$ , which marks the limit of the range of action of the inter-particle repulsion force. In (a) the chain-dotted line is proportional to  $\tilde{r}^{-0.65}$ .

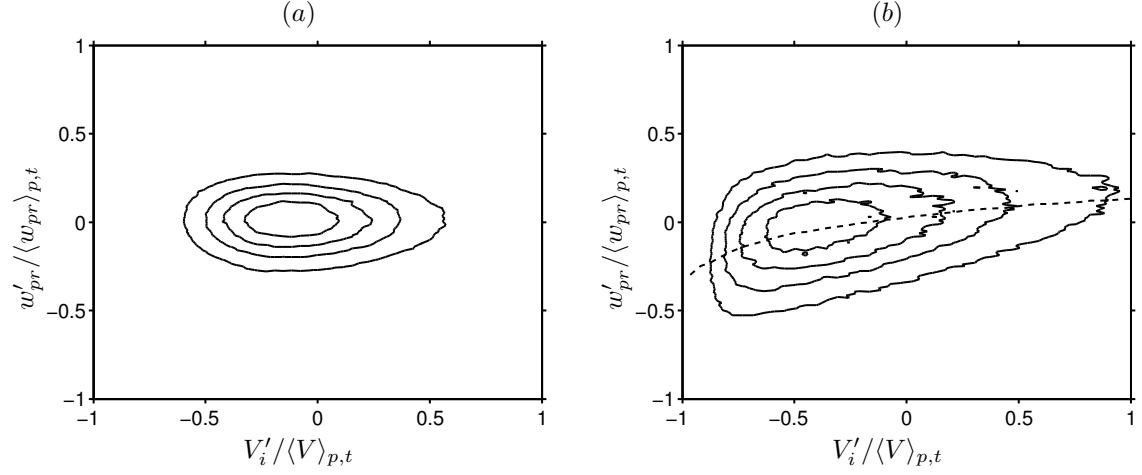


Figure 17: Joint p.d.f.s of the vertical component of the relative particle velocity fluctuations  $w'_{pr} = w_{pr} - \langle w_{pr} \rangle_{p,t}$  and the fluctuations of the Voronoi cell volumes  $V'_i = V_i - \langle V \rangle_{p,t}$  for: (a) case M121, (b) case M178. In both graphs the lines indicate contours at  $\{0.2, 0.4, 0.6, 0.8\}$  times the maximum number of occurrences. The dashed line in (b) indicates the conditional mean of  $w'_{pr}$  (conditional on  $V'_i$ ) under the same normalization, i.e.  $\langle w'_{pr} | V'_i \rangle$ .

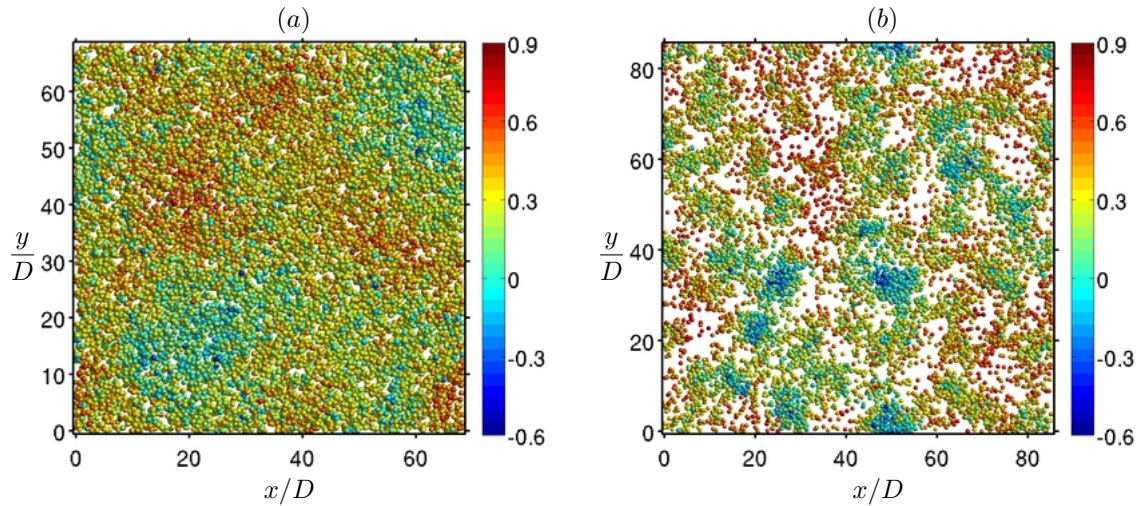


Figure 18: Top view of the particle locations at one instant in time. The particles are colored according to the fluctuation of their settling velocity  $w'_{pr} / \langle w_{pr} \rangle_{p,t}$ , where  $w'_{pr} = w_{pr} - \langle w_{pr} \rangle_{p,t}$ . (a) Case M121, (b) case M178.

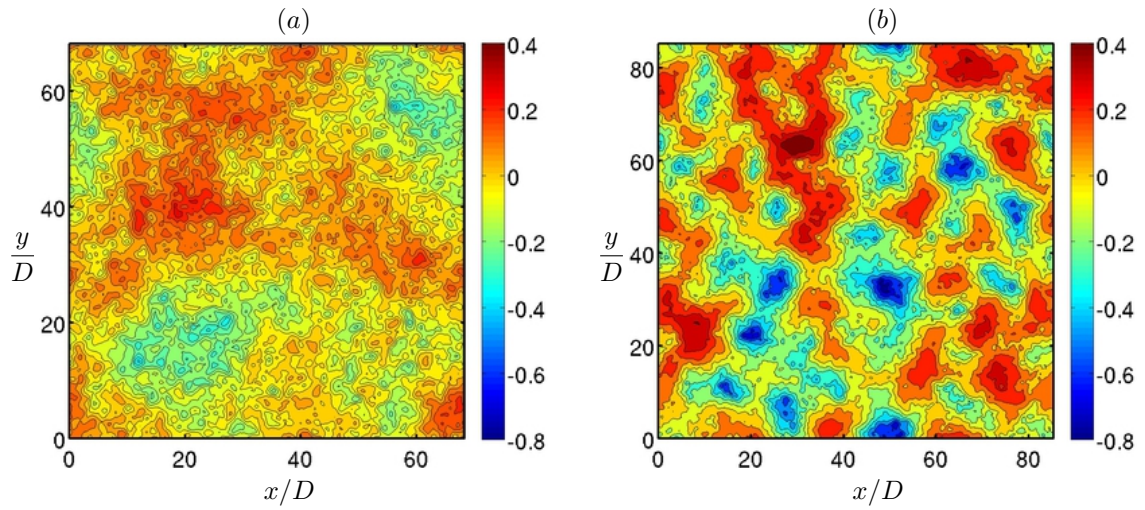


Figure 19: Instantaneous, vertically-averaged fluid velocity fluctuations normalized with the instantaneous box-average,  $\hat{w}'_f(x, y, t) / \langle w_f(\mathbf{x}, t) \rangle_{\Omega_f}$ , where  $\hat{w}'_f(x, y, t) = \langle w_f(\mathbf{x}, t) \rangle_z - \langle w_f(\mathbf{x}, t) \rangle_{\Omega_f}$ : (a) case M121, (b) case M178. The instants in time correspond to those in figure 18.

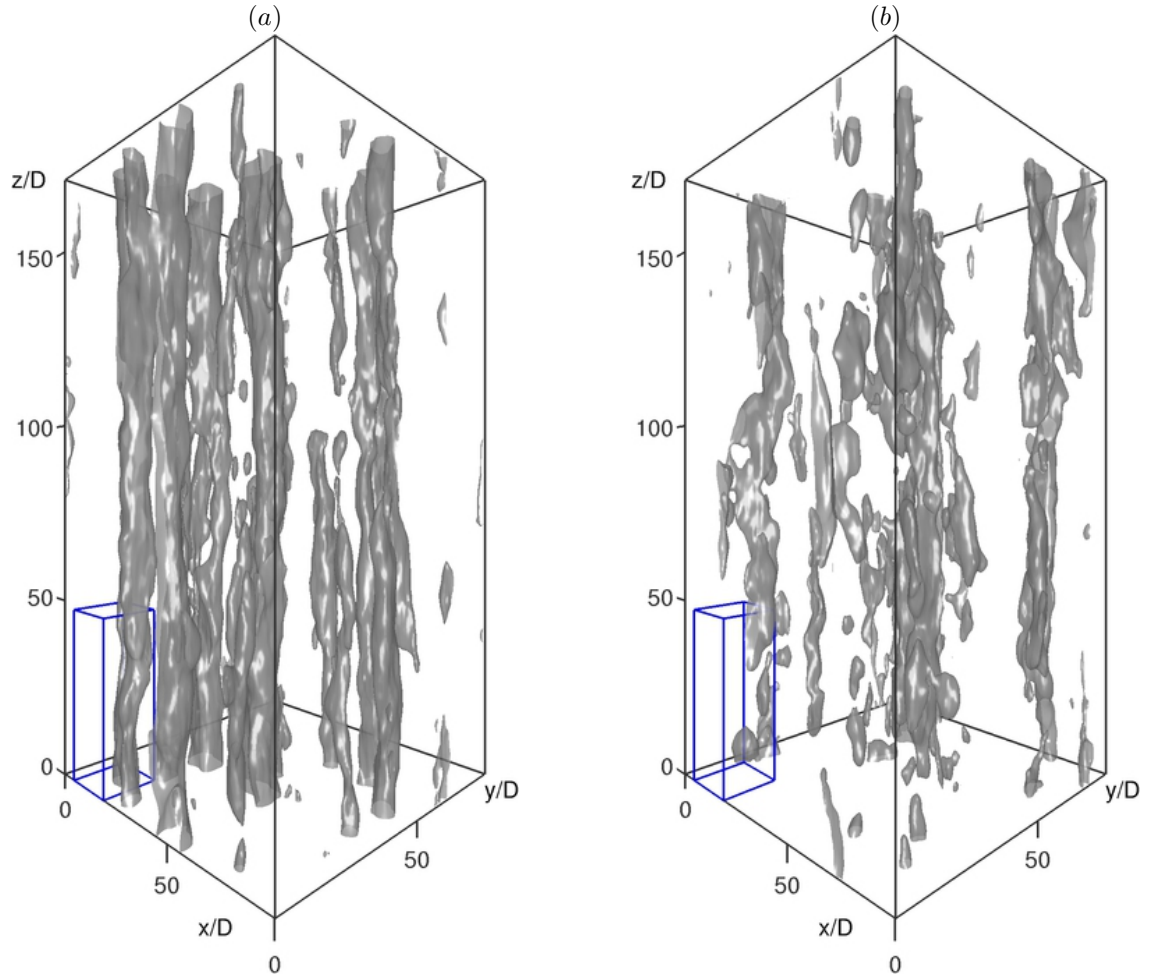


Figure 20: Iso-surfaces of the vertical fluid velocity fluctuations  $w'_f$  (with respect to the box-averaged value) in case M178 at one instant in the statistically stationary regime. The velocity field has been box-filtered with a filter width of  $5D$ . The graph in (a) shows a value of  $-0.4u_g$ , while (b) shows  $+0.4u_g$ ; these values are equivalent to  $\pm 1.05$  times the rms value of the unfiltered  $w'_f$  field. The small cuboid indicated by blue lines corresponds to the sub-volume shown in figure 21.



Figure 21: Iso-surfaces of the vortex eduction criterion proposed by [Jeong & Hussain \(1995\)](#) at a value of  $\lambda_2 = -0.25u_g^2/D^2$  (red color), showing a sub-volume of size  $16D \times 16D \times 48D$  in case M178. The flow data is taken at the same instant as in figure 20, where the present sub-volume is outlined. The large tube-like structure (indicated in grey color) shows an iso-surface of  $w'_f = -0.4u_g$ , as in figure 20(a). Gravity acts from top to bottom.

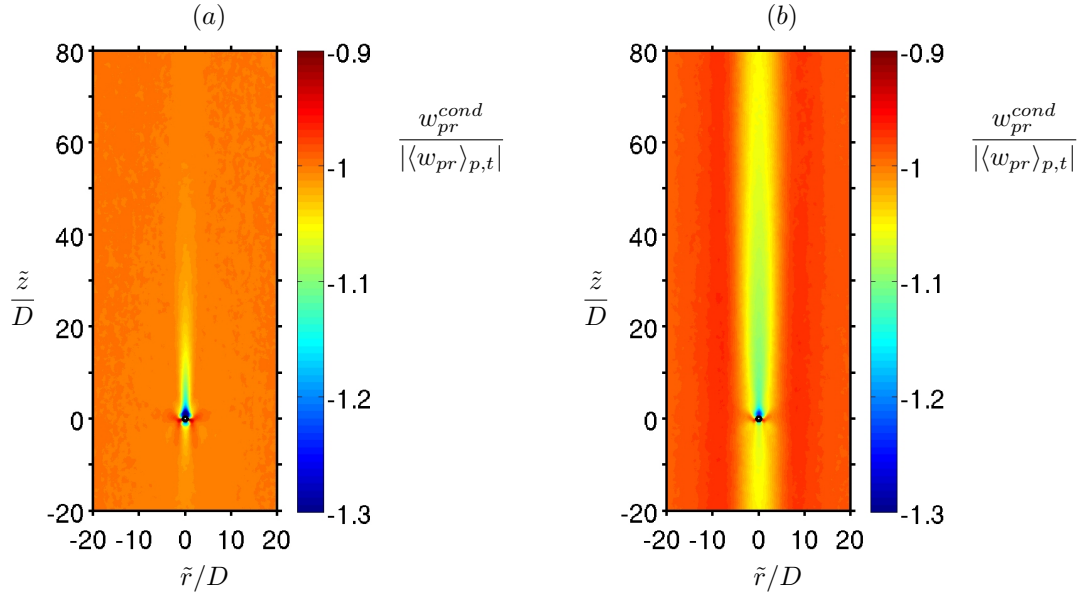


Figure 22: Spatial map of the particle-conditioned average value of the settling velocity,  $w_{pr}^{cond}$ , plotted as a function of the position  $(\tilde{r}, \tilde{z})$  with respect to a test particle (in a vertical plane): (a) case M121, (b) case M178.

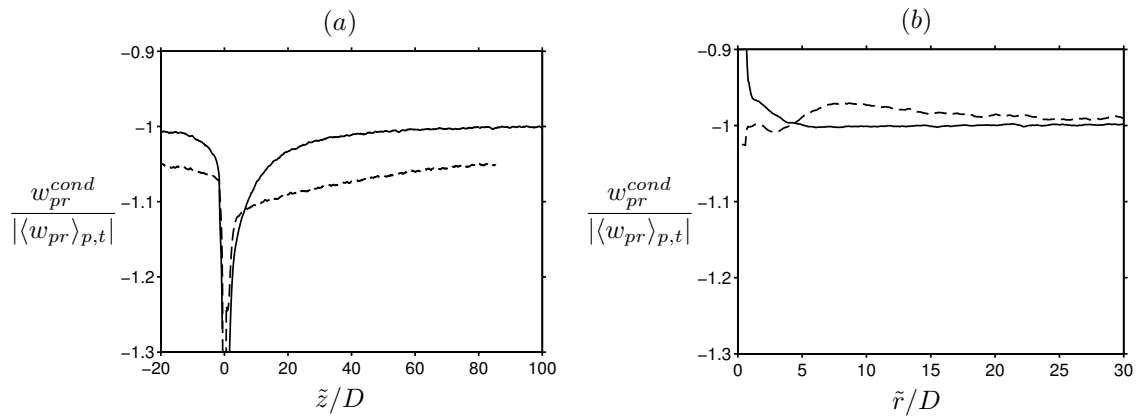


Figure 23: Variation of the particle-conditioned average value of the settling velocity (cf. figure 22) along two axes passing through the test particle: (a) vertical axis (with  $\tilde{r} = 0$ ), (b) horizontal axis ( $\tilde{z} = 0$ ). The line style indicates the flow cases: case M121 (solid line), case M178 (dashed).

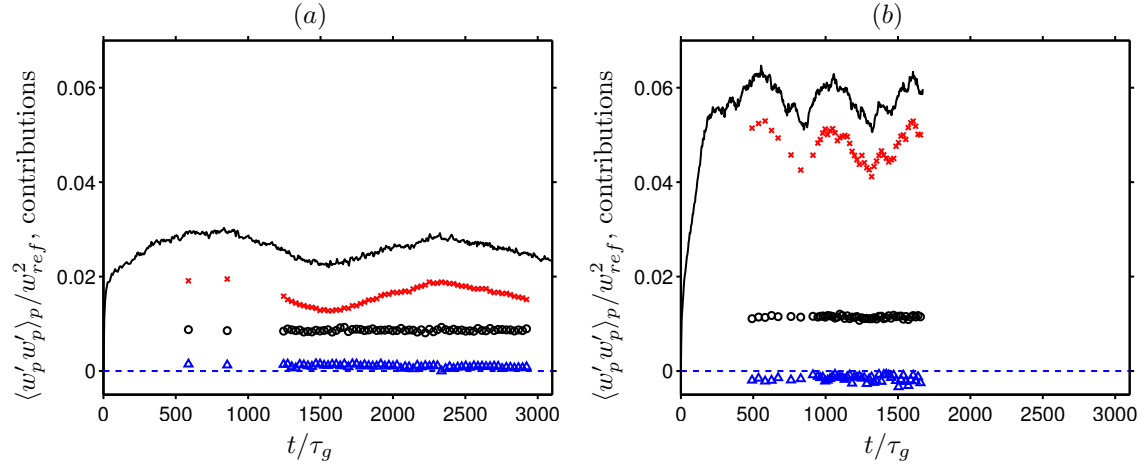


Figure 24: Variance of the vertical velocity of the particle phase,  $\langle w'_p w'_p \rangle_p$  (solid line), and its three contributions (cf. equation 8):  $\langle w_f^{S'} w_f^{S'} \rangle_p$  ( $\times$ ),  $\langle w_{pr}^{S'} w_{pr}^{S'} \rangle_p$  ( $\circ$ ),  $2\langle w_{pr}^{S'} w_f^{S'} \rangle_p$  ( $\Delta$ ). Graph (a) shows case M121, (b) shows case M178.

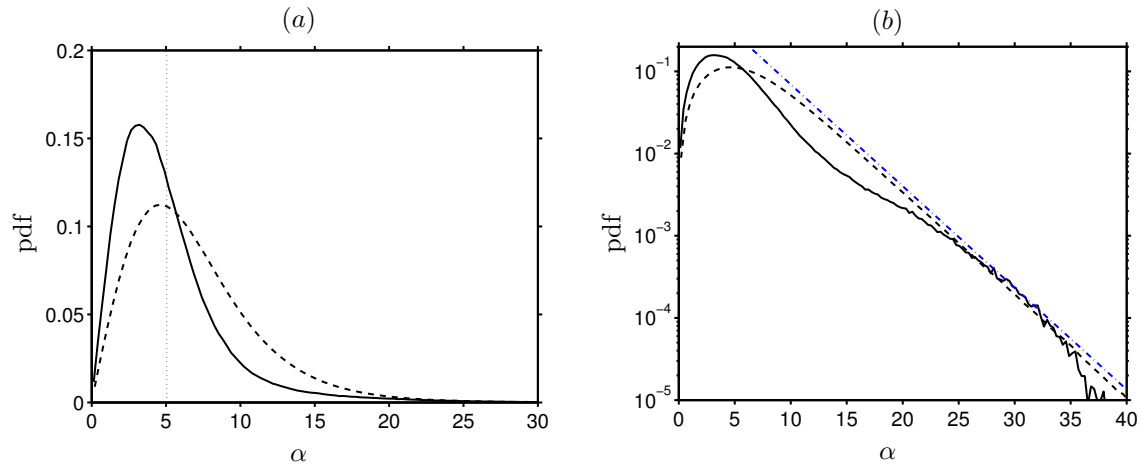


Figure 25: Probability density function of the angle  $\alpha$  between the relative particle velocity vector and the vertical axis, defined by  $\tan \alpha = (u_{pr}^2 + v_{pr}^2)^{1/2} / |w_{pr}|$ , measured in degrees, for case M121 (solid line) and case M178 (dashed line). The vertical dotted line denotes the value for an isolated sphere at the same density ratio and Galileo number as case M178. The graph in (b) shows the same data in semi-logarithmic scale. The chain-dotted line therein is proportional to  $\exp(-a\alpha)$  with  $a = 0.285$ .

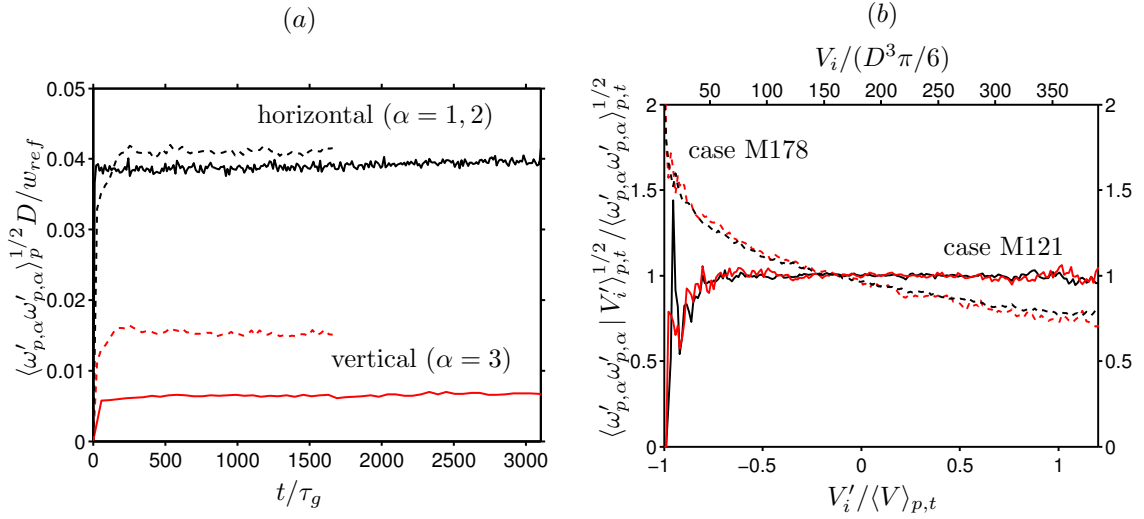


Figure 26: (a) Temporal evolution of the standard deviation of the angular velocity of the particle phase. (b) The conditional standard deviation of the angular velocity, conditional upon the Voronoi cell volume, normalized by the unconditional value. In the lower abscissa the fluctuation of the Voronoi cell volume, normalized by the mean value is used; in the upper abscissa, the Voronoi cell volume, normalized by the particle volume is used. Note that use of both scalings in a single graph is possible, since the mean value is the same in both flow cases. In both graphs the results for case M121 (solid lines) and case M178 (dashed lines) are shown; the components are indicated by black color ( $\alpha = 1, 2$ ) and red color ( $\alpha = 3$ ).